This is the accepted version. To access published version: https://doi.org/10.1016/j.ijheatmasstransfer.2022.122631

Assessing Effective Medium Theories for Conduction through Lamellar Composites

Omar Taleb,^{1,2} Daniel C. Barzycki,¹ Carlos Germosen Polanco,¹ Ralm G. Ricarte,¹ Daniel Hallinan Jr.^{1,2,*}

¹Florida A&M University-Florida State University College of Engineering, Department of Chemical & Biomedical Engineering, Tallahassee, FL 32310

²Aero-propulsion, Mechatronics, and Energy Center, Tallahassee, FL 32310

*Corresponding author email: dhallinan@eng.famu.fsu.edu

Abstract

In this study, we developed a numerical finite-difference model for 2D transient diffusion in lamellar structures. The explicit application is heat transfer, but it could equally be applied to dielectric constants, magnetic susceptibilities, electron/ion conduction, and mass diffusion as well. The control volume contains two phases A and B. The phases have different transport parameters. The modeling aims to evaluate the effect of grain size, grain boundaries, and phase contrast on apparent transport properties of composite materials, such as laminates, polycrystalline materials, and block copolymers, by examining a progression of increasingly complex structures. To validate the model, effective transport parameters of parallel and perpendicular structures from the numerical model are compared to analytical expressions. Effective Medium Theory provides an analytical expression in the limit of many, small, randomly oriented grains. The impact of coarse grains on transport is investigated. Specifically, the model is used to examine how the apparent transport parameters trend from the limit of a homogeneous material to small randomly oriented grains containing two different phases. The effective thermal conductivity (averaged over many random structures) was found not to be a function of grain size. However, the standard deviation decreased exponentially with decreasing grain size, reaching less than 2% variation for transport through 15 grains. Thus, the appropriate Effective Medium prediction is reliable for a surprisingly few number of grains, and connectivity of the more conducting phase is important only in coarse grains with significant contrast.

<u>Keywords:</u> Heterogeneous, Inhomogeneous, Numerical Model, Block Copolymer, Thermal Conductivity, Finite Difference Method.

I. <u>Introduction</u>

Lamellar composites may be considered as any multiphase material in which at least one phase has a roughly planar shape. For example, platelet-shaped particles, such as clay, and 2D materials, such as graphene dispersed in a polymer matrix, could be grouped in this category. These inorganic materials are essentially impermeable to molecules and ions but enhance thermal conductivity. The continuum approach used in this work assumes isotropic transport properties within each phase. Thus, it is more relevant to particles that impact macroscopic transport properties but are not intrinsically anisotropic within the particle, as opposed to 2D materials such as black phosphorus[1] that possess anisotropic transport properties within the particle. Also relevant to this work are polycrystalline materials, in particular semicrystalline polymers. Crystal lamellae contain well-ordered packing of polymer segments that are denser and less permeable/conductive to molecules/ions than the intervening amorphous regions.[2, 3] Conversely, thermal conductivity has been found to increase with degree of crystallinity in semicrystalline polymers.[4, 5] In fact, ultradrawn polyethylene has orders of magnitude greater thermal conductivity in the draw direction than in the transverse direction.[6] This is thought to be due to crystal alignment. Molecules containing liquid crystal moieties are yet another class of materials that can form lamellar structures.[7] A final example is block copolymers (BCPs). BCPs are a type of polymer in which chemically distinct monomer units are grouped in different blocks along the polymer chain. Under certain conditions, interactions between chemically distinct blocks along with molecular connectivity result in microphase separation into extraordinary structures.[8] When the blocks are of roughly equal volume fraction, the microphase separated structure is typically lamellar. The objectives of this study are to examine how transport is impacted by grain size, phase contrast, and connectivity of the more conductive phase, as well as to evaluate the most accurate effective medium expression for conduction in 2D lamellae.

Platelet particles and 2D materials are incorporated into polymers in order to slow transport of undesirable species (such as methanol in a fuel cell, lithium sulfides in a battery, or oxygen through a barrier material), improve thermomechanical properties (such as clay in nylon), and increase thermal conductivity (such as graphene in epoxy).[9-13] Although much more emphasis has been placed on thermal management applications in which high thermal conductivity is desired,[14] composites have also been designed for exceptional insulation properties[15] and for use as artificial muscles.[16] Similarly, block copolymer and semicrystalline materials have been used to control mechanical properties and transport of species such as gases, water, and ions. [17-20] One such example is the combination of rapid ion transport coupled with mechanical strength.[8]

Thermal transport in block copolymers has received limited attention. Mehra et al. reviewed the fundamentals of thermal transport in polymer composites, covered effective medium theories, and discussed design rules for material selection.[21] The application of BCPs to improve heat dissipation has been investigated by Alzina and coworkers.[22] They used metallization in a polymer containing active nanoelectronic and optoelectronic devices. Organic material can degrade if heat is not extracted efficiently. Therefore, it is important to measure and predict the thermal conductance of such polymer-based structures. Thermal transport in block copolymer films formed of polystyrene and poly(methyl methacrylate) (PS-b-PMMA) were studied by George et al.[23] Based on their results, the effective thermal conductivity of the BCP is not influenced by the film thickness nor phase separation this is due to the low thermal conductivity contrast between PS and PMMA. Phases with greater differences in thermal

conductivity than PS and PMMA might be expected to introduce a dependence of the effective thermal conductivity on structure. The possibility of selective incorporation of metal nanoparticles into one phase of a BCP[24-29] or in situ synthesis of metals within one phase of a BCP[30-32] are two exciting approaches for achieving nanostructured materials with large contrast in thermal conductivity, and it opens a new prospect in the control of heat transport for applications in thermal management.

Gas,[17, 33, 34] vapor,[18] and liquid[35] permeability through nanostructured membranes, as well as ion conduction have received much more attention than thermal transport. Due to their mathematical equivalence, additional insight into thermal transport through lamellar structures can be gained by considering these other types of transport. Petropoulos has reviewed effective medium equations for spherical and cylindrical inclusions as they pertain to the permeability of neutral molecules through two-phase structures.[36] Here, we focus on lamellar structures in BCPs. A number of studies have successfully analyzed gas transport through unaligned lamellar BCP membranes using either equations of Sax and Ottino[17, 34, 37], the Random Column Model (RCM)[33, 37], or both.

Effective medium theory defines a transport parameter of a homogeneous isotropic medium that behaves the same as a given composite material. The earliest and most prevalent effective medium theories (EMTs) have been derived by considering a heterogeneous material in a field and solving for the macroscopic average property of that material that recovers the appropriate field. Landauer has reviewed the earliest developments of EMTs.[38] The majority of effective medium expressions have been developed for spheres or ellipsoids dispersed in a matrix.[38, 39] Starting with Rayleigh, EMT models were also developed for cylinders.[39] The modern version of EMT is attributed to Bruggeman whose symmetrical expression has been generalized to ellipsoids, more than 2 phases, as well as 1, 2, and 3D.[38] For 2 phases with spheres in a matrix, the dimensionally generalized expression for the effective conductivity follows.

$$k_{EMT} = \frac{1}{2(d-1)} \left(\beta + \sqrt{\beta^2 + 4(d-1)k_A k_B} \right)$$
 (eq. 1)

where d is the dimensionality, and $\beta = (\phi_A k_A + \phi_B k_B)(d-1) - (\phi_A k_B + \phi_B k_A)$.

There are fewer studies that detail transport through lamellae. Cohen and coworkers developed RCM, which was originally applied numerically to gas permeation in BCPs.[33, 37] Like the current study, their model was built from series and parallel building blocks. For series conduction, transport must occur through both phases, and the effective thermal conductivity is a harmonic (volume fraction weighted) average of the thermal conductivity of the two phases.[40-42]

$$k_{series} = \left(\frac{\phi_A}{k_A} + \frac{\phi_B}{k_B}\right)^{-1}$$
 (eq. 2)

 k_{series} is the effective thermal conductivity for the series model. ϕ_A and ϕ_B are the volume fractions of phases A and B, respectively. k_A and k_B are the thermal conductivities of phases A and B, respectively. For parallel conduction, transport can occur through both phases simultaneously, and the effective thermal conductivity is a simple rule of mixtures.

$$k_{parallel} = \phi_A k_A + \phi_B k_B$$
 (eq. 3)

RCM studies focused on the limit of many grains, which prevents more in-depth comparison with the current work that focuses on few grains. An analytical expression for randomly oriented grains in RCM has been reported. [43] The analytical expression evaluates an integral over grain orientations, but it is unclear what is the appropriate upper limit of this integration, which renders the expression of limited utility. Another approach, also built using series and parallel building blocks, was reported by Sax and Ottino. [42] This too applies in the limit of random orientation of many grains. Based on Minelli et al. the equation for the effective thermal conductivity of a 3D complex geometry is [34]

$$k_{SO-EMT} = \frac{2}{3} k_{parallel} + \frac{1}{3} k_{series}$$
 (eq. 4 – a).

For a 2D complex geometry (Figure S1) it would be

$$k_{SO-EMT} = k_{SPA} = \frac{1}{2} k_{parallel} + \frac{1}{2} k_{series}$$
 (eq. 4 – b).

In 2D, the Sax and Ottino expression, k_{SO-EMT} , is equivalent to k_{SPA} , which is the arithmetic mean of k_{series} and $k_{parallel}$ that are taken from equation 2 and equation 3, respectively.[44, 45] Since these studies did not examine the effects of grain size nor alignment, we shift focus to ionic conductivity, where there has been the most extensive experimental effort. Using the terminology of polycrystalline materials, "grain" is used to refer to a region of coherently oriented lamellae.

Anisotropic ionic conductivity in lamellar structures has been observed in semicrystalline polymer electrolytes,[46, 47] graphene oxide-polymer composites,[47, 48] halographically polymerized polymers,[47, 49, 50] organic ionic plastic crystals,[51] smectic liquid crystals[52-54], and lamellar block copolymers[35, 55-60]. In these systems, structures composed of one ionically conductive layer alternate with a poorly or nonconductive layer. Alignment of the structures was achieved with a variety of approaches, including molecular interactions (especially surface interactions),[52, 53] applied stress to induce flow,[56] magnetic fields,[58] electric fields,[56] and solvent casting.[35, 57] In most cases, ionic conductivity parallel to the oriented layers was found to be dramatically greater than that perpendicular to the layers, i.e. 1 to nearly 4 orders of magnitude difference. In some cases, the improvement in parallel conductivity over randomly oriented grains was similar to that predicted by Sax and Ottino,[56, 58, 61] but in many cases the improvement was much greater than the prediction. [35, 52, 53, 55, 57] Moreover, conductivity has been found to trend proportionally[55] or inversely[62, 63] with grain size in different systems. Lack of knowledge regarding structural connectivity across grain boundaries and transport along grain boundaries is often implicated to describe disagreements such as these. Although measurement of transport through lamellar defects has been achieved with pulsed field gradient-nuclear magnetic resonance,[64] experimental measurement of transport in grain boundaries is extremely challenging, if not impossible at this time. This is due to numerous factors. For example, in soft materials, grain boundary structure is usually poorly defined and difficult to characterize. Lack of precise knowledge of grain boundary structure precludes accurate measurement of dynamics within them.

Analytical solutions for 1D transient conduction are possible for laminated structures, but are quite complicated for more than two layers.[65, 66] Steady-state analytical solutions are also possible for uniform spheres on a regular lattice and other periodic media, as well as random distributions of a discrete phase in a matrix of different conductivity.[67, 68] We are not aware of studies investigating more complex structures; this is likely due to the complexity or impossibility of analytical approaches.

The Finite Difference Method (FDM) is a powerful numerical technique to solve partial differential equations. Dusinberre used FDM to solve different heat transfer problems in his book.[69] Also, this method was used to develop a powerful code called Trump, by Edwards, to calculate transient and steady-state temperature distributions in multidimensional systems.[70] Claiborne et al. compared the results of several heat transfer computer codes when applied to a hypothetical nuclear waste repository. All the codes agreed within ±5%,[71] motivating the use of numerical methods.

This work uses a numerical model to examine how idealized structures affect apparent conductivity. In particular, diffusive thermal energy transport is modeled through increasingly complex arrangements of substructures. While the structures are motivated by BCPs, the findings are relevant to the other lamellar composites discussed above. While the model is developed explicitly for transient diffusion of thermal energy, the mathematical handling is equivalent for mass diffusion and electron/ion conduction.[65, 72] Table 1 shows the equations for different types of transport that could be applied in the same way as the thermal diffusion problem described here. The form of the governing equations for transient diffusion of heat, mass, momentum and ions are similar, with time derivatives on the left-hand side. The parameters multiplying the Laplacian operator (∇^2) and the dependent variables are different. In heat transport the variable is the temperature (T), and the parameter is thermal diffusion (α) where k is thermal conductivity, ρ is density, and C_p is specific heat. In mass transport the variable is concentration of species $i(c_i)$, and the parameter is molecular diffusion coefficient (D_i) . In momentum transport the variable is velocity (u), and the kinematic viscosity parameter (v) is the ratio of dynamic viscosity (μ) over ρ . In ion transport electrostatic interaction between charged components leads to more complicated expressions. The concentration of ion i (c_i) is related to the gradient of potential ($\nabla \phi$) via the heterogeneous reactions at the control volume boundaries. The ionic conductivity (κ) is related to the mobility of ion $i(u_i)$, its valence (z_i) , Faraday's constant (F), the gas constant (R), and T.

Table 1. Mathematical equivalence of transport of various types, including key coefficients, empirical flux relations, and transient diffusion equations.

Transport type	Transport Parameter [#]	Constitutive Flux Equation#	Governing Equation*		
Heat	Thermal diffusion $\alpha = \frac{k}{\rho C_p} \left[\frac{\text{cm}^2}{\text{s}} \right]$	Fourier's Law $q = -k\nabla T$ $\left[\frac{W}{cm^2}\right]$	$\frac{\partial T}{\partial t} = \alpha \nabla^2 T$		
Mass	Molecular diffusion $D_i \ [{ m cm^2/s}]$	Fick's 1 st Law $j_i = -D_i \nabla c_i$ $\left[\frac{\text{mol}}{\text{cm}^2 \text{ s}}\right]$	$\frac{\partial c_i}{\partial t} = D_i \nabla^2 c_i$		
Momentum ^a	Kinematic viscosity $\nu = \frac{\mu}{\rho} \left[\frac{\text{cm}^2}{\text{s}} \right]$	Newton's Law $\tau = \mu \nabla \mathbf{v}$ $\left[\frac{N}{cm^2}\right]$	$\frac{\partial \mathbf{v}}{\partial t} = \nu \; \nabla^2 \mathbf{v}$		
lon ^b	Ionic conductivity $\frac{\kappa}{F} = F \sum_{i} z_{i}^{2} c_{i} u_{i} \left[\frac{\text{mol}}{\text{V cm s}} \right]$ $u_{i} = \frac{D_{i}}{RT} \left[\frac{\text{mol cm}^{2}}{\text{V C s}} \right]$	Ohm's Law $i = \kappa \nabla \Phi$ $\left[\frac{A}{\text{cm}^2}\right]$	$\frac{\partial c_i}{\partial t} = \frac{\kappa}{F} \nabla^2 \Phi$		

^{*}Example metric units provided.

In this study, an FDM model of 2D transient diffusion in lamellar structures was implemented in MATLAB. The lamellar structure contains 2 phases, A and B, with different transport parameters. The goals of the modeling are 1) to evaluate the effect of grain size and grain boundaries on the apparent macroscopic conductivity by examining a progression of increasingly complex structures, 2) to evaluate the effectiveness, in idealized lamellar structures, of various EMT expressions that predict apparent conductivity, and 3) to examine the impact of phase contrast on heterogeneous transport. Starting with the simplest models in a homogeneous control volume, as well as horizontal and vertical lamellar structures, the numerical results are compared to exact (analytical) expressions in order to validate the custom numerical model. This research addresses the three goals and examines how the effective transport parameters trend from the limit of a perfectly ordered structure to that predicted by EMT expressions.

II. Methods section

Table 2 presents schematics of different structures that were modeled. The structure contains two phases. Phase A is shown in yellow, and phase B is shown in blue. The properties of the phases are reported in Table 3. Initially the entire region is at a constant temperature, T(x, y, t = 0) = 25 °C. The boundary conditions are specified in Figure 1 for dimensionless position, where it has a constant-temperature heat

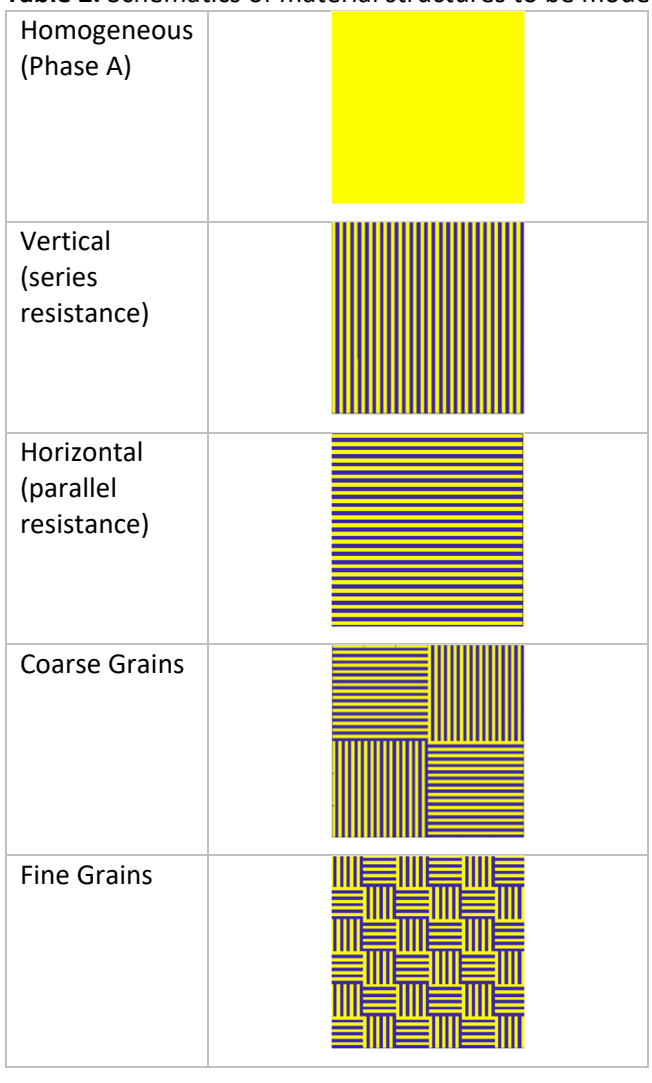
^{*}Subject to assumptions of no convective transport, no homogeneous reaction, and constant transport parameter.

^aGoverning equation assumes there is no pressure gradient.

^bFor simplicity of presentation, governing equation assumes no concentration gradient, as is the case for single-ion conduction. Ohm's Law is the more useful expression in this case. Note that I = VC.

source of $T=100~^\circ\text{C}$ at x=0, and a constant-temperature heat sink of $T=25~^\circ\text{C}$ at x=1. At y=0 and y=1 there is no flux. The given structure from Table 2 would occupy the control volume (CV) depicted in Figure 1, yielding a complete description of the given simulation. Our primary objective is to determine the heat flux at x=1 at steady state to determine the apparent thermal conductivity of the composite and compare to effective medium predictions to see the effect of grain size, connectivity of grain boundaries, and phase contrast on transport in an idealized system.

Table 2. Schematics of material structures to be modeled.



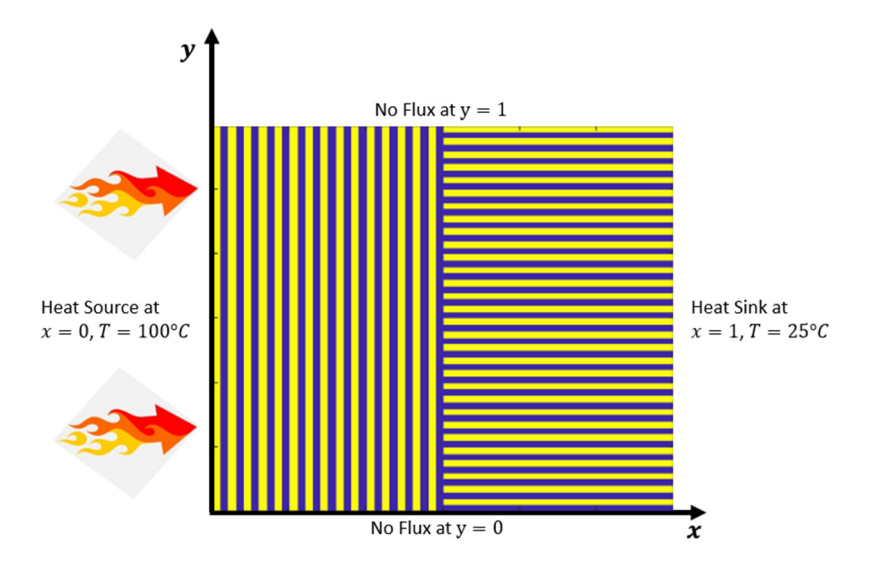


Figure 1. Example control volume, coordinate system, and boundary conditions.

Table 3. Material properties

Phase	k (W/m K)	$ ho C_p$ (N/m² K)	
Α	2	2×10^{-6}	
В	0.2	2×10^{-6}	

The governing equation for transient heat conduction without generation and without convection within the CV is

$$\frac{\partial(\rho C_p T)}{\partial t} = -\nabla \cdot q \quad \text{(eq. 5)}.$$

The accumulation of thermal energy term is equal to the negative of the divergence of heat flux, q. Fourier's Law defines q and is shown in equation 6 for flux in the x-direction.

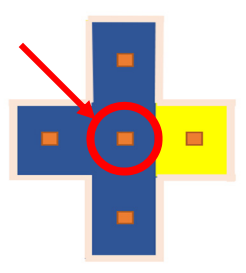
$$q_x = -k_x \frac{dT}{dx}$$
 (eq. 6)

Various types of boundary conditions could be applied, including constant temperature (Dirichlet conditions), no flux or constant heat source (Neumann conditions), and phase change (Robin conditions). For all simulations in this work, no flux boundary conditions have been used in the y-direction, which in dimensionless form is as follows:

At
$$y = 0$$
, $\frac{\mathrm{d}T}{\mathrm{d}y} = 0$

At
$$y = 1$$
, $\frac{\mathrm{d}T}{\mathrm{d}y} = 0$

These boundary conditions simplify the determination of effective thermal conductivity by only needing to consider macroscopic heat transfer in the x-direction. However, local transport in the y-direction is accounted for within the control volume in order to capture the 2D effect of the lamellar structure.



Schematic 1. Phase B in blue is the central node in contact with other Phase B nodes and a Phase A node depicted in yellow.

Using FDM requires that the governing equations and boundary conditions be discretized. Calculations at nodes that occur adjacent to an interface between phases must be considered in order to ensure that the FDM approach accurately captures transport. For this purpose consider heat flux q in phase B represented by the central blue grid point in Schematic 1, sharing an interface with phase A (node in yellow). All nodes are set in the middle of each block so that the phase properties at each node are well defined. The flux between the A and B nodes can be shown to obey the following equation.

$$q = -\frac{2k_A k_B}{k_A + k_B} \frac{T_B - T_A}{\Delta x} \quad \text{(eq. 7)}$$

Equation 7 is derived in Appendix A. It begins with conservation of energy and assumes that there is neither resistance to heat transfer nor accumulation at the interface. This means that heat flux is equal on both sides of A/B interfaces. As shown in Appendix A, the harmonic mean of thermal conductivities that appears in equation 7 is derived by solving for the temperature of the A/B interface.

This same approach can be used if an additional resistance to heat transfer exists at the interface, R_{int} . In such a case, it can be assumed that the temperature on either side of the interface is not the same,[39] but that the flux through the interface is the same as that on either side, i.e. that there is no accumulation at the interface. Then the flux would be

$$q = -\frac{2k_A k_B}{k_A + k_B + \frac{2k_A k_B R_{int}}{\Delta x}} \frac{T_B - T_A}{\Delta x}$$

It is apparent from this expression that interfacial resistance would dominate in the limit as R_{int} become much larger than k_A and k_B . Since the purpose of the present study is to examine the impact of structure on conduction, R_{int} has been taken to be zero so as not to convolute interfacial effects, including Kapitza resistance, with structural effects. Such effects that are likely to be material specific and appear to become significant in grain sizes below 50 nm would be better examined with molecular dynamic simulations.[73] Enhancement of thermal conductivity due to nanotwin boundaries could be captured empirically by using a negative R_{int} , but it would be more appropriate to use molecular dynamic simulations.[74]

Considering multiple phases and multiple nodes, equation 5 can be written

$$\rho_i C_{\mathrm{p,i}} \left(\frac{\partial \mathbf{T}}{\partial \mathbf{t}} \right)_{i,j} = -\nabla \cdot q_{i,j} \text{ (eq. 8),}$$

where i and j will be used to refer to nodes that could be phase A or phase B. It is assumed 1) that ρ , C_p , and k are constants, 2) that transport occurs in two-dimensions (the x and y directions), 3) that there is no convection, and 4) that there is no homogenous heat generation.

In order to implement FDM, the time derivative was discretized following equation 9, where n is number of time iterations.

$$\left(\frac{\partial T}{\partial t}\right)_{i,j} = \frac{T_{i,j}^{n+1} - T_{i,j}^{n}}{\Delta t} \quad (eq. 9)$$

The divergence of flux was discretized according to equation 10 - a.

$$\nabla \cdot q_{i,j} = \frac{\partial q_x}{\partial x} + \frac{\partial q_y}{\partial y} = \frac{q_{i+1,j} - q_{i-1,j}}{\Delta x} + \frac{q_{i,j+1} - q_{i,j-1}}{\Delta y} \text{ (eq. 10 - a)}$$

Although equation 10 - a appears to be a centered space discretization, a '2' does not belong in the denominator because the flux is being calculated a half step before or after position i, j, such that the divergence of flux spans only 1 node step.

Equations 9 and 10-a are inserted into equation 8 to give equation 10-b.

$$\rho_{i}C_{p,i}\frac{T_{i,j}^{n+1} - T_{i,j}^{n}}{\Delta t} = -\left[\frac{q_{i+1,j} - q_{i-1,j}}{\Delta x} + \frac{q_{i,j+1} - q_{i,j-1}}{\Delta y}\right] \quad (eq. 10 - b)$$

Explicitly, each term in equation 10 - b for $q_{i+1,j}$, $q_{i-1,j}$, $q_{i,j+1}$, and $q_{i,j-1}$ can be generalized from equation 7. By explicitly using the thermal conductivity of each node. The following generalized flux expressions apply regardless of whether there is an interface present or not.

$$q_{i+1,j} = \frac{-2k_{i,j}}{1 + \frac{k_{i,j}}{k_{i+1,j}}} \frac{\mathbf{T}_{i+1,j}^{\mathbf{n}} - \mathbf{T}_{i,j}^{\mathbf{n}}}{\Delta x}$$

$$q_{i-1,j} = \frac{-2k_{i-1,j}}{1 + \frac{k_{i-1,j}}{k_{i,j}}} \frac{\mathbf{T}_{i,j}^{\mathbf{n}} - \mathbf{T}_{i-1,j}^{\mathbf{n}}}{\Delta x}$$

$$q_{i,j+1} = \frac{-2k_{i,j}}{1 + \frac{k_{i,j}}{k_{i,j+1}}} \frac{\mathbf{T}_{i,j+1}^{n} - \mathbf{T}_{i,j}^{n}}{\Delta y}$$

$$q_{i,j-1} = \frac{-2k_{i,j-1}}{1 + \frac{k_{i,j-1}}{k_{i,j}}} \frac{\mathbf{T}_{i,j}^{n} - \mathbf{T}_{i,j-1}^{n}}{\Delta y}$$

Each term in equation 10-b is replaced by its equivalent above yielding equation 11.

$$T_{i,j}^{n+1} = T_{i,j}^{n} + \frac{\Delta t}{\rho_{i,j} C_{p,i,j}} \left[\left(\frac{2k_{i,j}}{1 + \frac{k_{i,j}}{k_{i+1,j}}} \frac{T_{i+1,j}^{n} - T_{i,j}^{n}}{\Delta x^{2}} + \frac{-2k_{i-1,j}}{1 + \frac{k_{i-1,j}}{k_{i,j}}} \frac{T_{i,j}^{n} - T_{i-1,j}^{n}}{\Delta x^{2}} \right) + \left(\frac{2k_{i,j}}{1 + \frac{k_{i,j}}{k_{i,j+1}}} \frac{T_{i,j+1}^{n} - T_{i,j}^{n}}{\Delta y^{2}} + \frac{-2k_{i,j-1}}{1 + \frac{k_{i,j-1}}{k_{i,j}}} \frac{T_{i,j}^{n} - T_{i,j-1}^{n}}{\Delta y^{2}} \right) \right] (eq. 11)$$

The validity of equation 11 can be verified by setting all $k_{i,j}$ equal to show that the usual Forward Time Centered Space FDM expression for a homogeneous CV is recovered.

To calculate the temperature after the first time step, all the nodes are set to 25 °C initially. When the first time iteration starts, the temperature of the nodes at x=0 are equal to 100 °C, and at x=1 they are set to 25 °C. The temperature after each time iteration is calculated explicitly, and the boundary conditions in the x and y directions are reinforced for each new time iteration. As described by Rice and Do, the nodes are shifted by a half step (to force their location to not coincide with interfaces).[75]

$$x_i = (i - \frac{1}{2})\Delta x$$
 and $y_i = (i - \frac{1}{2})\Delta y$

In equation 11, the term x_i does not appear. Therefore, this shifting only needs to be applied in the boundary conditions. Below are the new x-direction boundary conditions after shifting.

$$\frac{T(0,y) + T(0 + \Delta x, y)}{2} = 373 K$$

$$\frac{T(1,y) + T(1 - \Delta x, y)}{2} = 298 K$$

The discretized boundary conditions in the y direction are not affected by shifting.

$$T(x,0) = T(x,0 + \Delta y)$$

$$T(x,1) = T(x,1 - \Delta y)$$

The stability condition for the explicit FDM in 2D is

$$F_0 = \frac{\alpha_i \Delta t}{\Delta x^2} \le \frac{1}{2} \quad \text{(eq. 12)}$$

To ensure stability, the following constraint was applied to the time step size:

$$\Delta t = \min\left(\frac{1}{4} * \frac{\Delta x^2}{\alpha_A}; \frac{1}{4} * \frac{\Delta x^2}{\alpha_B}\right) \text{ (eq. 13)}$$

$$\Delta x = \frac{W}{N_x - 1}$$

$$\Delta y = \frac{H}{N_y - 1}$$

$$\alpha_A = \frac{k_A}{\rho_A C_{p,A}}, \qquad \alpha_B = \frac{k_B}{\rho_B C_{p,B}}$$

The step size in the x-direction, Δx , is set equal to Δy because W and H are equal. As shown in Figure 2(a), W is the overall width of the CV, and H is the CV height. H and W have been set to 10^{-4} cm in all simulations. N_x and N_y , the number of nodes in the x and y directions, respectively, are also equal.

The temperature of each node is calculated through a matrix $T_{i,j}^n(N_x,N_y)$ using equation 11, where i represents the x index and j represents the y index. The final value of n, for all cases other than the homogeneous case, is $t^*/\Delta t$, where t^* is the time for the system to reach steady state, which has been estimated as

$$t^* = \max\left(\frac{W^2}{\alpha_A}; \frac{W^2}{\alpha_B}\right) = \frac{W^2}{\alpha_B}.$$

Upon reaching steady state, the effective thermal conductivity, k_{eff} , of each FDM simulation was determined. First, the flux in the x direction at $x=10^{-4}$ cm and every y position was calculated as $q_{x,j}=-k_{m,j}\frac{T_{m,j}-T_{m-1,j}}{\Delta x}$, where m is the final node in the x direction and j is the y-direction index. These fluxes were averaged to yield $\langle q_x \rangle = \frac{\sum_{j=1}^p q_{x,j}}{p}$, where p is the final node in the y direction. Finally, k_{eff} was calculated according to

$$k_{eff} = \frac{\langle q_x \rangle W}{\Lambda T}$$

The temperature difference across the CV in the x direction, i.e. between x=0 and $x=10^{-4}$ cm, is $\Delta T=(373-298)=75$ K. Thus, k_{eff} is readily determined from $\langle q_x \rangle$.

Figure 2(a) shows an example of how the 2 phases are separated. In this example, there are 60 lamellae in the horizontal direction. Figure 2(b) shows how each phase contains the same number of nodes, which are designated by orange squares. The thickness of each lamella is $17 \, \mathrm{nm}$, and it is divided into 5 nodes. The nodes are shifted a half step as described above. This was necessary because the appropriate thermal conductivity is ill-defined at the interface between two phases that have different values. The number of lamellae and number of nodes per lamella were chosen to maintain a constant number of total nodes in each direction. So, the total structure has $300 \times 300 = 90,000 \, \mathrm{nodes}$. This was found to yield smooth, accurate temperature profiles while maintaining acceptable simulation time. Figure 2 (c) helps to clarify the index notation of the nodes used in equation 11.

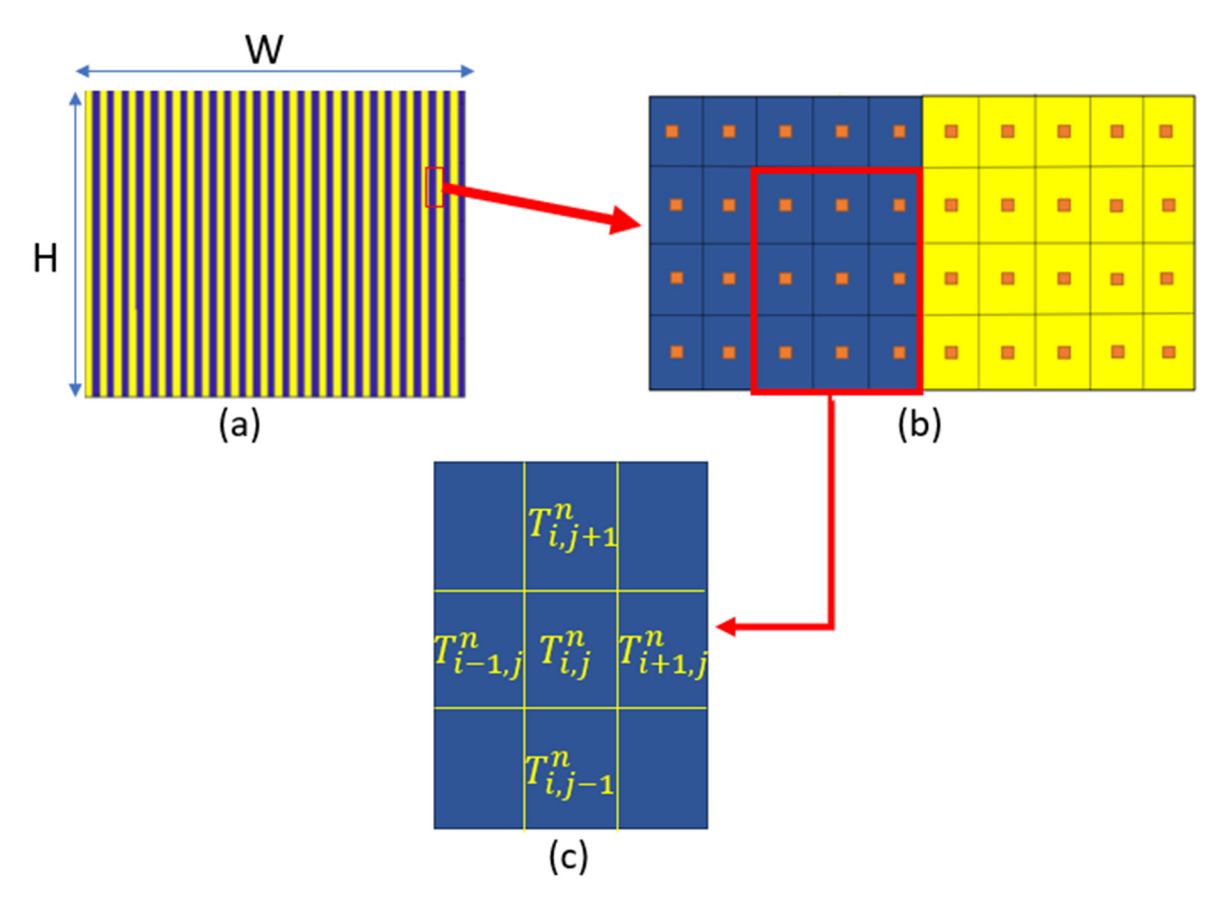


Figure 2. (a) Example CV with 2-phase structure, (b) Indication of location and number of nodes within each phase, and (c) Index notation for FDM calculations at the central node.

The most challenging part was to generate a random distribution of structures when combining series and parallel grains in complex combinations and to assign transport properties to nodes within grains. The orientation of grains was determined by a function that randomly generated 0 or 1. Vertical grains were assigned a value of 0, and horizontal grains were assigned a value of 1. For example, in the 6×6 structure shown in Figure 3, the random function generated each block 0 or 1 to give the output structure as shown in the figure. Based on the specific structure, a set of functions defined matrices containing the material properties of each node at position i,j. Each function had inputs from the main code to define the size and the number of grains of the composite. Based on these inputs the function generated matrices such as k (for thermal conductivity related to each phase) and ρC_p (for the product of density and specific heat in each phase). These matrices were used in the calculation of the temperature in equation 11. By explicitly using the transport properties of each node in equation 11, it applies regardless of whether there is an interface present or not. In other words, as long as there are matrices containing the transport properties associated with the structure being simulated, it is not necessary to otherwise account for the presence of interfaces within the FDM calculations. This is a powerful aspect of the specific FDM approach developed here.

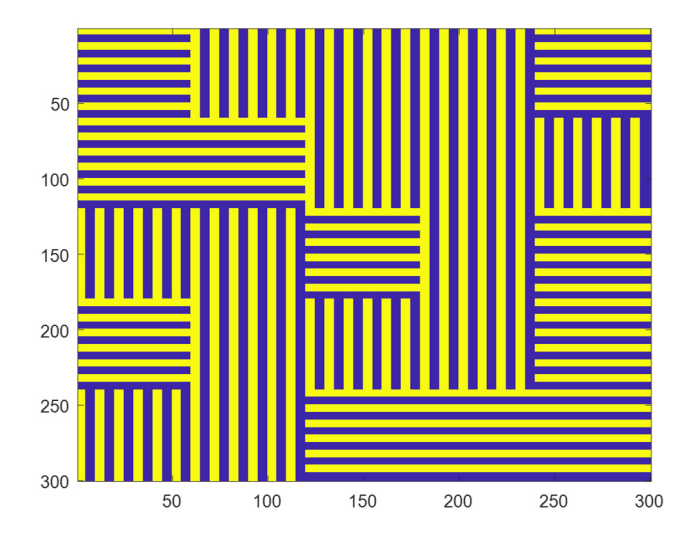


Figure 3. Characteristic 6×6 structure with node number specified on each axis.

III. Results and Discussion

1. Homogeneous Material

The result of the numerical model was compared to an analytical solution, with the same boundary conditions and assumptions. 1D is sufficient for the homogeneous case due to the no flux boundaries conditions in y-direction and the boundary conditions in the x-direction not being a function of y.

$$\rho C \frac{\partial T}{\partial t} = -\nabla \cdot q \quad (eq. 14)$$

$$\rho C \frac{\partial T}{\partial t} = k \frac{\partial^2 T}{\partial x^2} \quad (eq. 15)$$

$$E.C: \quad x = 0$$

$$T_0 = 100^{\circ}C$$

$$x = 10^{-4}$$

$$T_W = 25^{\circ}C$$

$$t = 0$$

$$T = 25^{\circ}C$$

The solution of equation 15 is derived in Appendix A, and the result is

$$\frac{T - T_W}{T_0 - T_W} = \left(1 - \frac{x}{W}\right) - 2\sum_{n=0}^{\infty} \frac{\sin\left(n\pi\frac{x}{W}\right)}{n\pi} e^{-(n\pi)^2 \frac{t}{t^*}} \quad \text{(eq. 16)}.$$

Temperature profiles generated from equation 16 are presented in Figure 4 as curves, where $t^* = \frac{W^2}{\alpha_A}$ and 10,000 terms are included in the series summation. At time equal to 0, the temperature is equal to 25 °C throughout the control volume, except at x=0 where it is 100 °C as defined by the boundary condition. The flux and temperature profiles have been examined for increasing times up to steady state at t^* . As shown in Figure 4, the temperature at x=0 is 100 °C and decreases with increasing x until it reaches 25 °C at x=1, according to the boundary condition there. The steepness of the temperature profile near x=0 decreases with increasing time until the steady state is reached, which is a linear profile. This is due to the fact that before reaching steady state the material is gaining heat from the source and with time the material will be saturated with the maximum amount of thermal energy that it can hold

subjected to these boundary conditions. At steady state, i.e. at t^* , the temperature profile is a line of $T = -75\frac{x}{10^{-4}} + 100$, and the flux is constant.

Using the finite difference method described in the experimental section, a homogeneous control volume of phase A material was modeled. The same boundary conditions described above are applied. The numerical model ran from time zero up to t^* , the same as that used for the analytical solution. The temperature profiles resulting from the FDM calculations are presented in Figure 4 as open circles. The steady state temperature profile is reached at time equal to t^* , and it agrees with the analytical one. The results of FDM agree with the analytical solution at all times shown in Figure 4, which validates the numerical model. For the homogeneous case, $\langle q_x \rangle = 15050 \frac{\rm W}{\rm cm^2}$, so $k_{eff} = \frac{15050*10^{-4}}{75} = 0.02 \frac{\rm W}{\rm cm\,K} = 2 \frac{\rm W}{\rm m\,K}$, which is equal to the specified thermal conductivity of phase A, another validation of the model.

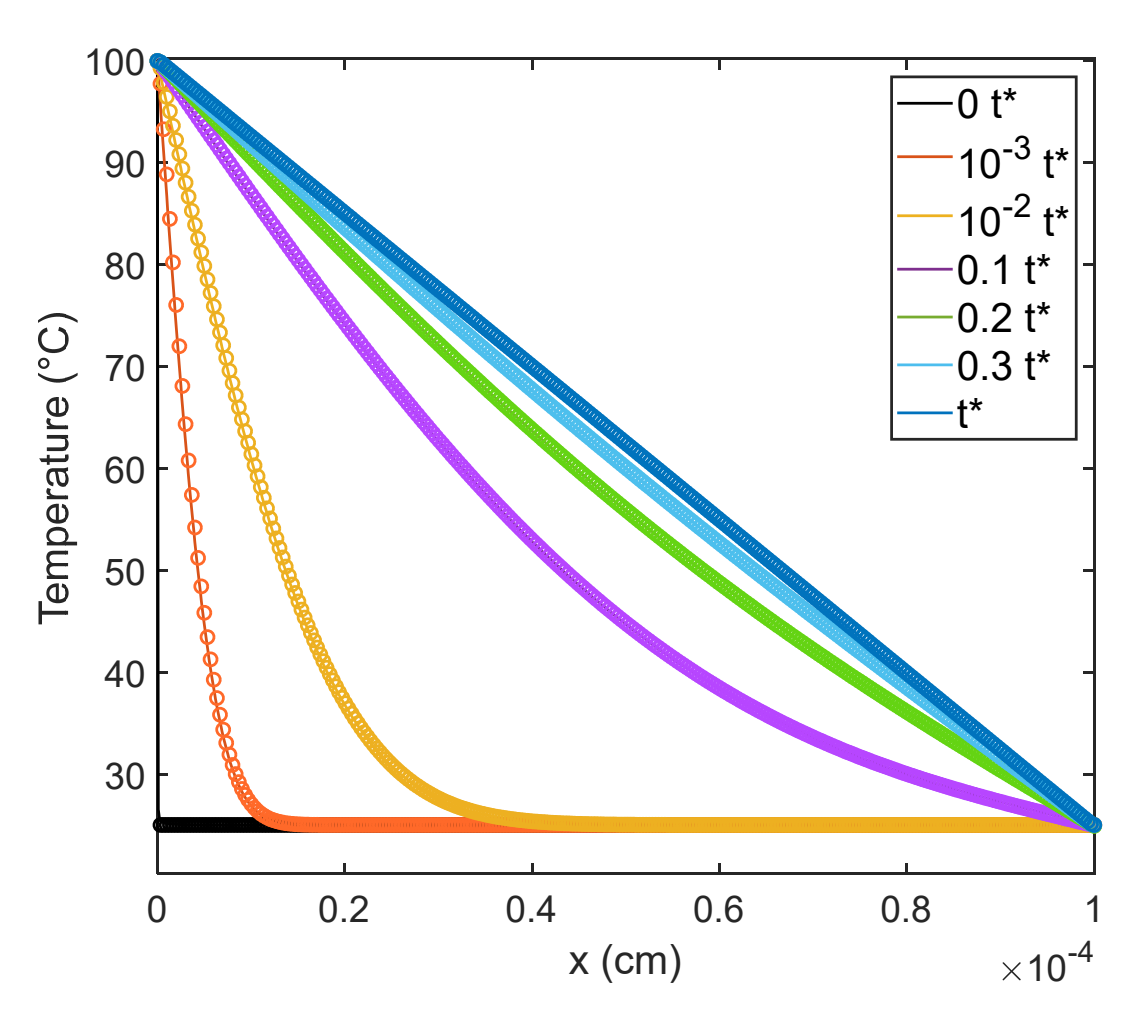


Figure 4. Temperature profiles of homogeneous CV at times noted in legend from the analytical solution (curves) and from the finite difference model (open circles).

2. Vertical, Horizontal, and Diagonal Lamellae

Two structures were used to validate the finite difference model applied to heterogeneous structures: 1) vertical lamellae in which heat flux in the x-direction is via series resistance depicted in Figure 5(a) and 2) horizontal lamellae in which x-direction heat flux is via parallel resistance shown in Figure 5(d). In this work, the volume fractions of phase A and phase B are equal at 0.5. For series conduction (vertical lamellae), equation 2 predicts the effective thermal conductivity as $k_{series} = \left(\frac{0.5}{2} + \frac{0.5}{0.2}\right)^{-1} = 0.36 \frac{W}{m \, K}$. From FDM, $\langle q_x \rangle = 2736.4 \frac{\mathrm{W}}{\mathrm{cm}^2}$, and $k_{eff} = \frac{2736.4 \frac{\mathrm{W}}{\mathrm{cm}^2} * 10^{-4} \mathrm{cm}}{(373 - 298) \ \mathrm{K}} = 0.0036 \frac{\mathrm{W}}{\mathrm{cm} \ \mathrm{K}} = 0.36 \frac{\mathrm{W}}{\mathrm{m} \ \mathrm{K}}$, which is equal to the prediction of k_{series} . The temperature profiles at different times up to steady-state are shown in Figure 5(b). At times less than $0.5t^*$, the temperature did not reach steady state, and it decreased from 373 to 298 K with a steep slope. The steady state is reached at $0.5t^*$, where the temperature decreased from 373 to 298 K with variable slope due to the variation of thermal conductivity as a function of x. In other words, the temperature gradient is smaller in the A phase (that has higher thermal conductivity) than in the B phase (that has lower thermal conductivity), because the flux through both phases must match at steady state. In other words, the slope of the temperature profile changes on going from one phase to another due to their different thermal conductivities. Finally, a 2D graph of the temperature as a function of x and y is provided in Figure 5(c). For clarity, the grid for all 2D profiles is shown for every 10th data point. In Figure 5(c) this prevents the variable slope from being apparent. The variable slope is apparent in Figure S2, a larger figure with every 5th data point shown

For parallel conduction (horizontal lamellae), equation 3 predicts $k_{parallel}=0.5*2+0.5*0.2=1.1~\frac{\rm W}{\rm m~K}$. From FDM, $\langle q_x\rangle=8277.7~\frac{\rm W}{\rm cm^2}$, and $k_{eff}=\frac{\langle q_x\rangle_W}{\Delta T}=\frac{8277.7~\frac{\rm W}{\rm cm^2}*10^{-4}{\rm cm}}{75~{\rm K}}=0.011~\frac{\rm W}{\rm cm~K}=1.1~\frac{\rm W}{\rm m~K'}$ which is equal to the analytical prediction of $k_{parallel}$. The temperature profiles at different times up to and including steady-state are shown in Figure 5(e). At $0.01t^*$, the temperature does not reach steady state, and it decreases with a sharp slope from 373 to 298 K. Interestingly, steady state is achieved more rapidly in the horizontal structure than in the vertical lamellae, related to the higher k_{eff} of the former. Steady state is reached at $0.1t^*$ in the horizontal lamellae demonstrated by its overlapping with $5t^*$ in Figure 5(e) and having a fixed slope equal to $(298-373)/10^{-4}=-7.5\times10^5~{\rm K/cm}$. Steady state is achieved before t^* , because t^* has been defined using the thermal diffusivity of phase B (the phase with lower thermal conductivity). Finally, a 2D graph of the temperature as a function of x and y is provided in Figure 5(f). The agreement of FDM results for both vertical and horizontal lamellae with analytical predictions is a validation that the FDM model can accurately capture diffusive transport in heterogeneous media. Note that the analytical expressions for series and parallel conduction are only strictly valid for 1D transport,[67] which is the case in these single grain calculations due to the no-flux boundary conditions in the y direction.

A third structure composed of 60 diagonal lamellae is shown in Figure 5(g). The heat flux calculated from FDM is $4702.1 \frac{W}{cm^2}$, and k_{eff} is $0.62 \frac{W}{m\,\mathrm{K}}$. To the best of our knowledge, there is no analytical expression to predict the thermal conductivity in such a structure. The diagonal structure can be decomposed into series and parallel components, but it is not clear what is the appropriate average. An arithmetic mean yields $k_{SPA} = 0.5k_{series} + 0.5k_{parallel} = 0.73 \frac{W}{m\,\mathrm{K}}$. On the other hand, a harmonic mean yields $k_{SPH} = \left(\frac{0.5}{k_{series}} + \frac{0.5}{k_{parallel}}\right)^{-1} = 0.55 \frac{W}{m\,\mathrm{K}}$. The FDM result is somewhat lower than the average of these limits, which is $k_{avg} = 0.5k_{SPA} + 0.5k_{SPH} = 0.64 \frac{W}{m\,\mathrm{K}}$. As will be discussed in more detail later, effective

medium approximations such as these tend to over predict effective transport coefficients when there is a significant difference between the parameter values of the phases. In this case, the parameters of the phases differ by an order of magnitude. The temperature profile of the diagonal structure at different times is a function of x and is presented in Figure 5(h). Also, a 2D representation of the temperature as a function of x and y is presented in Figure 5(i).

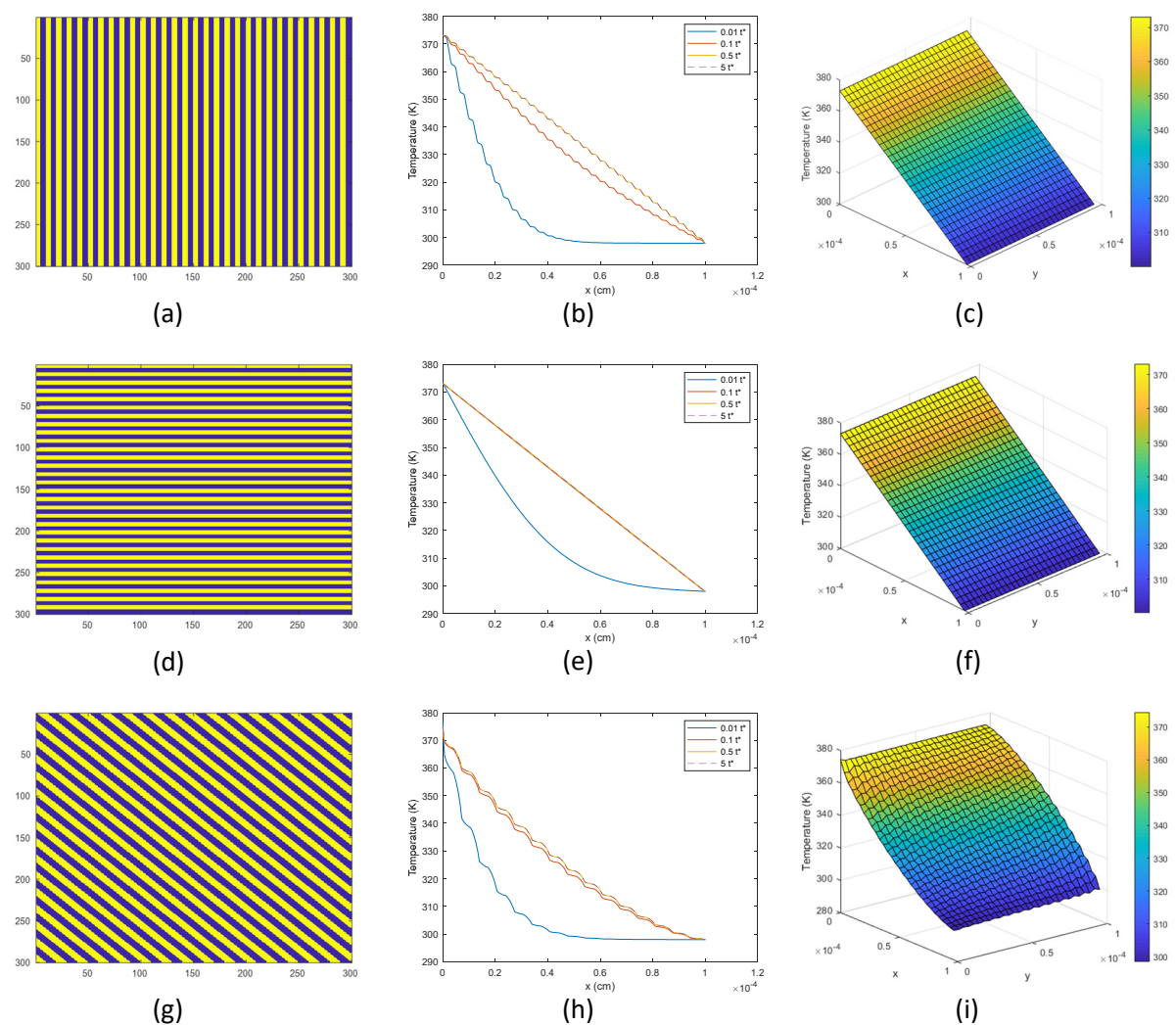


Figure 5. (a) Series structure. (b) Series temperature profile as a function of x at y = 1. (c) Series 2D temperature profile. (d) Parallel structure. (e) Parallel temperature profile as a function of x at y = 1. (f) Parallel 2D temperature profile. (g) Diagonal structure. (h) Diagonal temperature profile as a function of x at y = 1. (i) Diagonal 2D temperature profile.

3. Complex Geometry

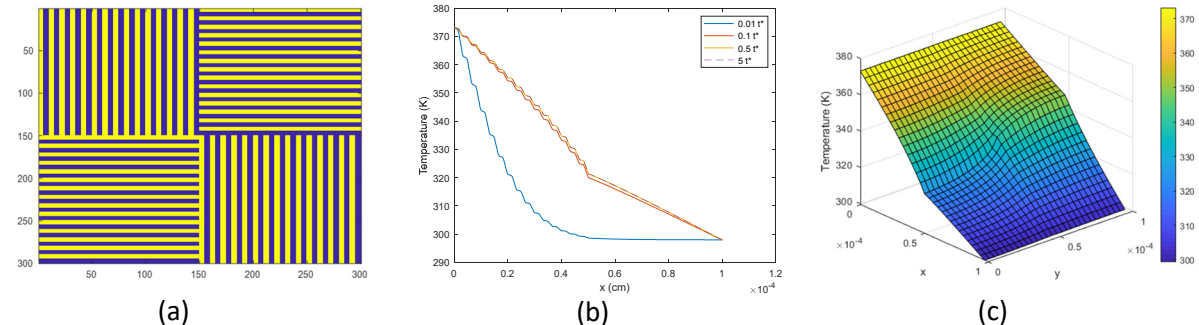
Using the knowledge gained in modeling the vertical and horizontal lamellae, the two models are combined in complex geometries. Complex geometries were constructed from square subregions containing either vertical or horizontal lamellae. Subregions will be referred to as grains. The complexity of the structure was increased from 2x2 to 15x15 grains. The orientation of each grain (vertical or horizontal) is randomly assigned. The same boundary conditions described in the experimental section

are applied. To study the effect of the grain size on k_{eff} , the number of grains and number of lamellae per grain are changed in each structure so that the lamellar thickness remains the same. As shown in Table 4, as the number of grains increase the number of lamellae per grain decrease, i.e. the grain size decreases. The 2x2 structure has 4 grains each containing 30 lamellae. In the 3x3 structure, there exist 9 grains of 20 lamellae each. In the 5x5 structure, there are 25 grains of 12 lamellae each. Finally, the 6x6 structure contain 36 grains each with 10 lamellae; the grains in the 10x10 structure contain 6 lamellae; and the grains in the 15x15 structure each contain 4 lamellae. So, the domain size (thickness of a pair of lamellae) of all these structures is 33 nm. In all cases, each lamella contains 5 nodes so that all structures contain 300×300 nodes.

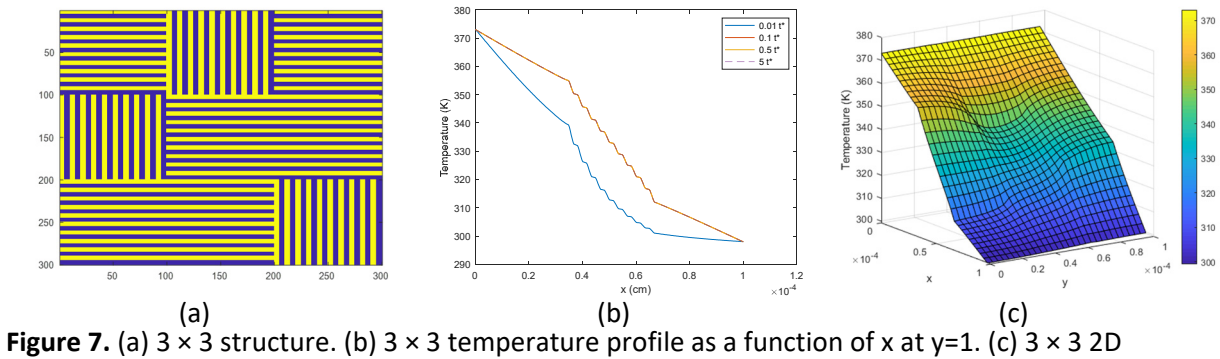
Table 4. Details of complex geometries modeled. The first column describes the size of all structures modeled in this study. The second column shows the total number of grains in the entire structure. The third column includes the number of lamellae in each grain. The fourth column shows the grain size. The last column is the number of nodes in each lamella. The number of nodes is 300 in each direction. This can be seen by multiplying the fifth column with the third column with the number of grains in one direction, i.e. 5*30*2 for the 2x2 structure.

Structure size	# Total Grains	# Lamellae	Grain Size	# Nodes	
		per grain	(nm)	per lamella	
2x2	4	30	500	5	
3x3	9	20	333	5	
5x5	25	12	200	5	
6x6	36	10	167	5	
10x10	100	6	100	5	
15x15	225	4	67	5	

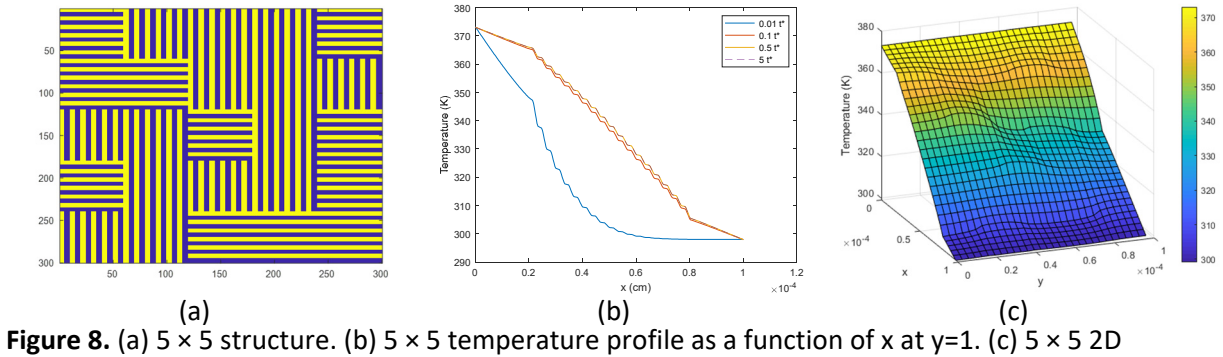
A characteristic set of the different structures are shown in Figures 6 to 11, starting with 2×2 and ending with 15×15 . At least five different random structures were simulated at each grain size. The depiction of every simulated structure can be found in the Supporting Information. In Figures 6 to 11, part (a) shows a characteristic structure, part (b) shows the temperature profile as a function of x at y=1 for several times up to steady state, and part (c) shows the steady-state temperature profile in 2D as a function of x and y.



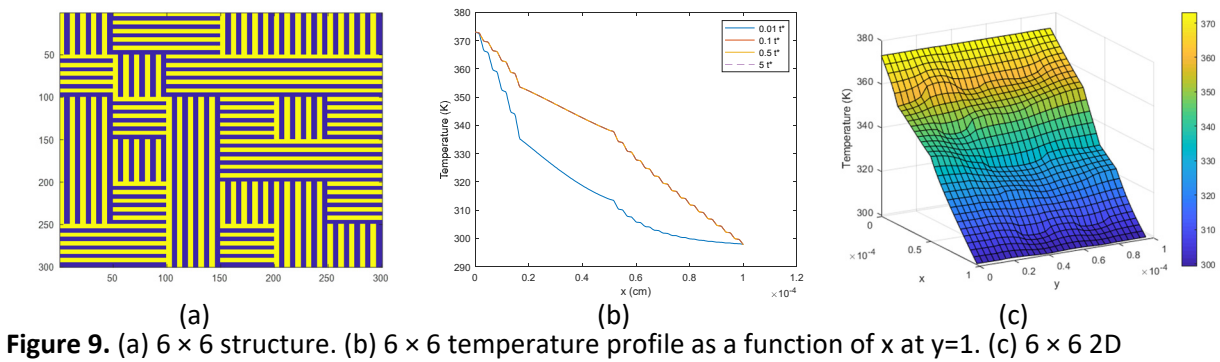
(a) (b) (c) Figure 6. (a) 2×2 structure. (b) 2×2 temperature profile as a function of x at y=1. (c) 2×2 2D temperature profile.



temperature profile.



temperature profile.



temperature profile.

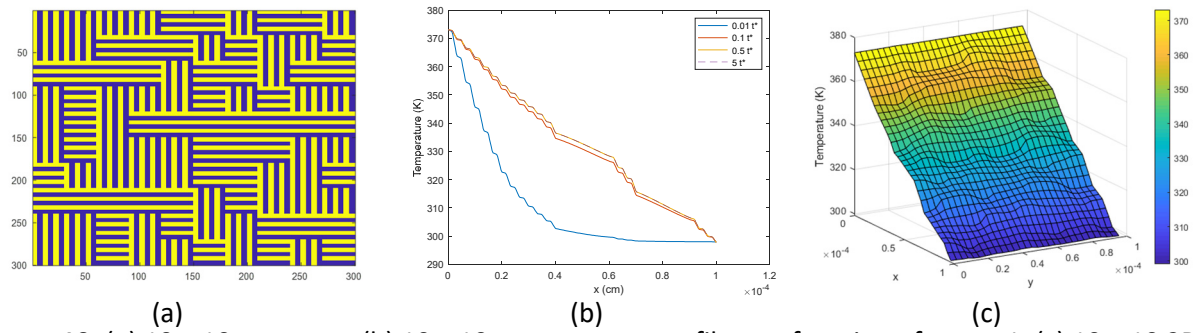


Figure 10. (a) 10×10 structure. (b) 10×10 temperature profile as a function of x at y=1. (c) 10×10 temperature profile.

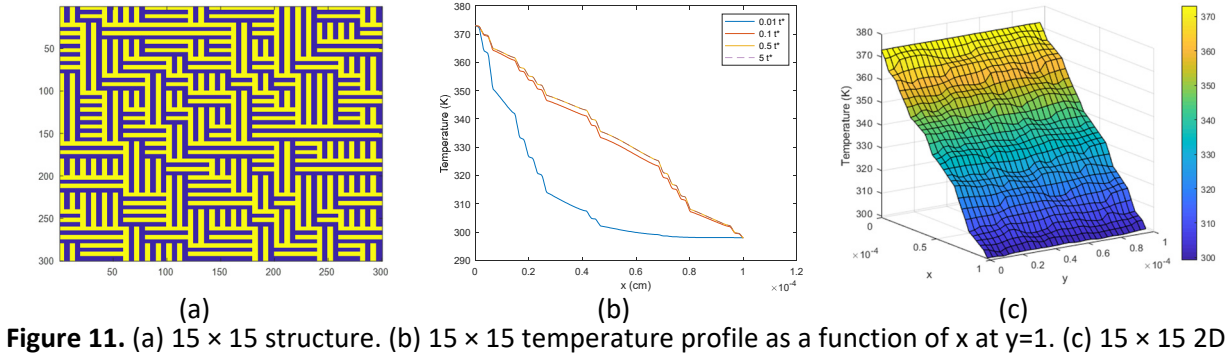


Figure 11. (a) 15×15 structure. (b) 15×15 temperature profile as a function of x at y=1. (c) 15×15 2D temperature profile.

The 6 × 6 structure (Figure 9) is taken as an example. The temperature profile as a function of x at y=1 is shown at different times in Figure 9(b). From the temperature profile the steady state is reached at 0.5t*, due to the lack of variation of the temperature profile with further increase in time. In addition to the visual check for steady-state, the heat flux at x=0 and x=1 are calculated, and the values agree to within $\pm 1\%$ indicating that steady state has been approximately reached. This check was conducted for all simulations and is shown in Table B1 of Appendix B. In Figure 9(c) the 2D steady-state temperature is shown. The time progression of the 2D profile is shown in Video S1 of the supporting information. It helps visualize the importance of heat transfer between phases on the transient development of the 2D temperature profile. In other words, Video S1 shows the impact of structure on transient heat conduction. Video S1 shows how the temperature increases in different parts of the structure at different rates, due to the difference in thermal properties and phase A connectivity in those regions. The effective thermal conductivity of the 6 × 6 structure of Figure 9 is $0.64 \frac{W}{m \, \text{K}}$, based on $\langle q_x \rangle = 4.2268 \times 10^3 \frac{W}{\text{cm}^2}$. The calculated thermal conductivity is lower than that predicted by Sax and Ottino's effective medium theory, i.e. k_{SPA} , which in 2D is $0.73 \frac{W}{m \, \text{K}}$.

The effective thermal conductivity of each simulation is reported in Table B1 along with the steady-state check described above. It was notable that all the results were below the predicted value of Sax and Ottino's EMT expression for all the grain sizes with only a few exceptions. The average effective thermal conductivity for each grain size, along with the specific structures that yielded the minimum and maximum k_{eff} are reported in Table 5. For the 2 × 2 grain size, $\langle k_{eff} \rangle = 0.64 \pm 0.12 \frac{\rm W}{\rm m~K}$. In the 2 × 2 structures of random generation, the maximum effective thermal conductivity was $0.84 \frac{\rm W}{\rm m~K}$ for structure 2 × 2(5). Refer

to the supporting information for a schematic of the structure. This was the first exception where the effective thermal conductivity calculated from FDM is higher than the one calculated from Sax and Ottino's EMT expression. The minimum effective thermal conductivity is $0.54 \, \frac{\rm W}{\rm m\, K}$ for structure 2 × 2(4). This variation between the maximum and minimum is due to which phase comprises the grain boundary, which plays an important role in determining effective thermal conductivity and will be discussed shortly. For the 3 × 3 grain size, $\langle k_{eff} \rangle = 0.656 \pm 0.10 \, \frac{\rm W}{\rm m\, K}$. In the 3 × 3 structures of random generation, the maximum effective thermal conductivity is $0.76 \, \frac{\rm W}{\rm m\, K}$ for 3 × 3(5), which is the second exception where the FDM result is higher than Sax and Ottino's EMT prediction. For the 5 × 5 grain size, $\langle k_{eff} \rangle = 0.636 \pm 0.10 \, \frac{\rm W}{\rm m\, K}$. In the 5 × 5 structures of random generation, the maximum effective thermal conductivity is $0.76 \, \frac{\rm W}{\rm m\, K}$ for 5 × 5(4), which is the third and final exception where the FDM result is higher than Sax and Ottino's EMT prediction. For the 6 × 6 grain size, $\langle k_{eff} \rangle = 0.624 \pm 0.05 \, \frac{\rm W}{\rm m\, K}$. For the 10 × 10 grain size, $\langle k_{eff} \rangle = 0.672 \pm 0.025 \, \frac{\rm W}{\rm m\, K}$. Finally, the 15 × 15 structures have an average effective thermal conductivity $\langle k_{eff} \rangle = 0.624 \pm 0.011 \, \frac{\rm W}{\rm m\, K}$.

Table 5. Summary of effective thermal conductivity as a function of grain size, where 2×2 has the largest grains and 15×15 has the smallest grains. The average and standard deviation of all randomly generated structures for a given grain size are reported, as well as the instances that yielded the minimum and maximum values. Refer to the supporting information for the minimum and maximum structures.

Grain size	$\langle k_{eff} \rangle$	Minimum	k_{eff}^{min}	Maximum	k_{eff}^{max}
Grain Size	(W/m K)	structure	(W/m K)	structure	(W/m K)
2 × 2	0.640 ± 0.120	2 × 2(4)	0.54	2 × 2(5)	0.84
3 × 3	0.656 ± 0.100	3 × 3(4)	0.51	3 × 3(5)	0.76
5 × 5	0.636 ± 0.100	5 × 5(2)	0.51	5 × 5(4)	0.76
6 × 6	0.624 ± 0.050	6 × 6(2)	0.56	6 × 6(4)	0.69
10 × 10	0.672 ± 0.025	10 × 10(3)	0.64	10 × 10(5)	0.70
15 × 15	0.624 ± 0.011	15 × 15(2)	0.61	15 × 15(4)	0.64

These results are summarized graphically in Figure 12, where $\langle k_{eff} \rangle$ can be seen to vary around a value of $0.63 \frac{\rm W}{\rm m~K}$, which is similar to that for a single diagonal grain $0.62 \frac{\rm W}{\rm m~K}$. Moreover, $\langle k_{eff} \rangle$ of the 15 × 15 structure is essentially the same as the FDM result for a single diagonal grain. The average of all multigrain simulations (2 × 2 through 15 × 15) is 0.642 ± 0.074 W/m K. This value agrees remarkably well with k_{avg} , the average of k_{SPA} and k_{SPH} . Remember that k_{SPA} is the arithmetic mean of series and parallel conduction, while k_{SPH} is the harmonic mean of series and parallel conduction.

$$k_{avg} = \frac{1}{2} \left[\frac{k_{series} + k_{parallel}}{2} + \frac{2}{\frac{1}{k_{series}} + \frac{1}{k_{narallel}}} \right] = \frac{k_{series}^2 + 6k_{series}k_{prallel} + k_{parallel}^2}{4(k_{series} + k_{parallel})}$$

Expressed explicitly in terms of k_A and k_B , it is

$$k_{avg} = \frac{\left(\frac{\phi_a}{k_a} + \frac{\phi_b}{k_b}\right)^{-1} + (\phi_a k_a + \phi_b k_b)}{4} + \frac{1}{\left(\frac{\phi_a}{k_a} + \frac{\phi_b}{k_b}\right) + (\phi_a k_a + \phi_b k_b)^{-1}}$$

As indicated by Figure 12, this recursive average appears to be the best prediction for two-phase lamellar systems with significant contrast, i.e. large difference in transport parameters of the two phases. The recursive average approach is a logical approach to build an effective medium expression from simple building blocks: series and parallel conduction. Take the upper left grain of Figure 6(a) as an example. It contains phase A and B in series configuration (for conduction in the x direction). In turn, the grain is in series with a parallel grain (upper right grain). It is also in parallel with a parallel grain (lower left grain). For more complex grain structures, the recursive averaging process could be conducted ad infinitum. Let us call k_{SPA} the first arithmetic mean recursion and k_{SPH} the first harmonic mean recursion. Then, k_{avg} is the second arithmetic mean recursion. For a contrast of 10, it agrees with the second harmonic mean for 1 significant figure. By the third recursion, arithmetic and harmonic averages agree up to 4 significant figures. For four recursions, they agree up to 8 significant figures. The recursions converge to the geometric mean.[76, 77] In other words, the better approach is the following:

$$k_{SPG} = \left(k_{series}k_{parallel}\right)^{1/2}$$
. (eq. 17)

The sensitivity of this recursive average approach to phase volume fraction has not been examined in this work, where $\phi_A = \phi_B = 0.5$ in all cases.

Using series and parallel building blocks is quite powerful because simple expressions can be used without sacrificing generality. For an arbitrary number of phases,

$$k_{parallel} = \sum \phi_i k_i$$

$$k_{series} = \left[\sum \frac{\phi_i}{k_i}\right]^{-1}$$

As was cleverly proposed by Chaudhary and Bhandari, [78] the geometric mean can also be generalized to account for non-random distribution of series and parallel

$$k_{eff} = k_{parallel}^n k_{series}^{1-n}$$
. (eq. 18)

Of course, n = 1/2 for a random distribution. Equation 18 is a valid equation for thermal conductivity because it satisfies Woodside and Messmer's requirement for 2 phases that [79]

$$\left(\frac{dk_{eff}}{dk_{parallel}}\right)_{k_{parallel}=k_{series}} = \phi_{parallel}.$$

It is worth emphasizing that the recursive averaging approach dictates that the series and parallel transport parameters be used in the geometric mean, not the transport parameters of the two phases. The latter approach, first proposed by Woodside and Messmer, occurs in Bruggeman's expression in the specific case of 2D with equal volume fractions ($\phi_{parallel} = \phi_{series} = 0.5$), but it does not yield the same value as equation 18 if there are more than 2 phases.

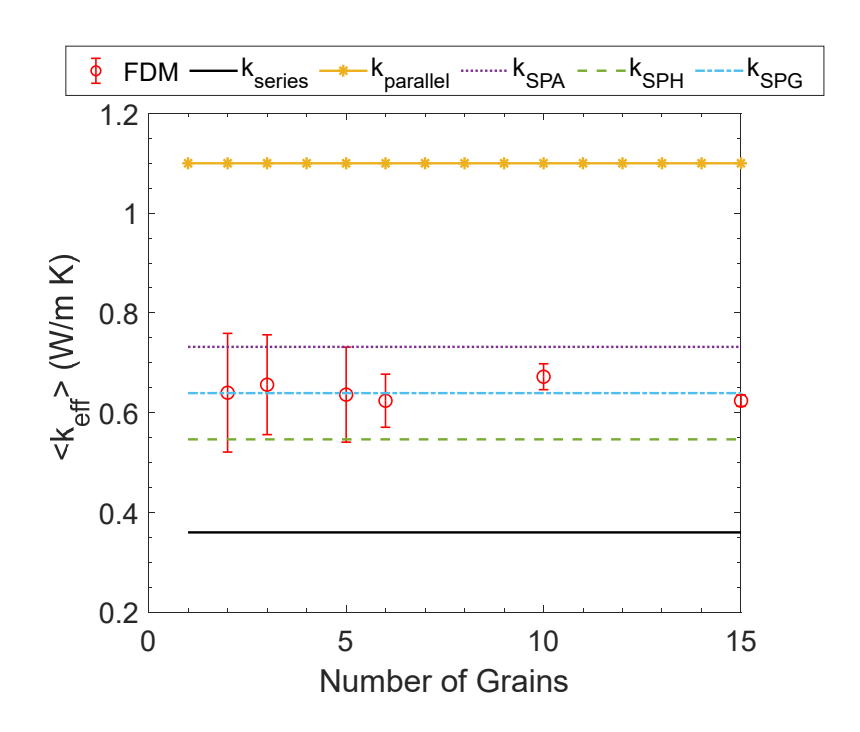


Figure 12. Average effective thermal conductivity, $\langle k_{eff} \rangle$, versus number of grains.

It is worthwhile to note that in practice, e.g. in experimental measurements of effective transport parameters, the structure is not known in nearly the detail that can be achieved with the modeling approach used here. Although grains in series and parallel in Figure 6(a) were used to motivate the recursive averaging approach, knowledge of the exact structure is not actually needed to implement recursive averaging. What the exact structure will impact is how well effective-medium predictions agree with experimental measurement. As shown in Table 5 and in Figure 12, the standard deviation of $\langle k_{eff} \rangle$ decreases with decreasing grain size. It is 0.12 W/m K for the largest grains (2 × 2) and decreases in a more or less exponential fashion with number of grains, as shown in Figure S3. For the smallest grains studied (15 × 15), the standard deviation of $\langle k_{eff} \rangle$ is an order of magnitude smaller at 0.011 W/m K. Specific manifestations of large grain structures have greater potential to diverge from effective-medium predictions than do smaller grain structures. Exactly this result has been observed by Romanenko and coworkers in plastic crystal electrolytes,[51] where rapidly crystallized samples contained smaller randomly oriented grains with small standard deviation of ionic conductivity. On the other hand, slow cooling resulted in larger, more oriented grains and much larger variation in conductivity. Thus, the specific structure plays a greater role in large grains and could, at least partially, explain counterintuitive effects such as the decrease of ionic conductivity in lamellar block copolymers with increasing grain size.[62] In other words, because there is greater variability from one specific structure to another in larger grains, the standard deviation of the thermal conductivity increases with increasing grain size.

It was notable how significantly certain features of specific structures impacted the effective thermal conductivity. In particular, k_{eff} was strongly affected by the connectivity of the more conductive phase, especially on the side closest to the heat source. This was observed in two structures that were identical except for a difference in the boundary between grains. This was seen in 2 examples. Structures from the first example, referred to as $2 \times 2(4)$ and $2 \times 2(6)$, are shown in Figure 13 (a) and (b), respectively. The

boundary between grains at x=0.5 is blue (phase B, $k_B=0.2\frac{W}{m\,\mathrm{K}}$) in $2\times2(4)$ with a thermal conductivity of $0.54\frac{W}{m\,\mathrm{K}}$. Whereas, in $2\times2(6)$ the boundary between the grains at x=0.5 is yellow (phase A, $k_A=2\frac{W}{m\,\mathrm{K}}$), which increases the overall thermal conductivity to $0.55\frac{W}{m\,\mathrm{K}}$. The second example is $2\times2(1)$ and $2\times2(2)$, shown in Figure 14. The grain boundary at $0\le x\le0.5$ and y=0.5 changes from blue in $2\times2(1)$ to yellow in $2\times2(2)$. In this case, the effective thermal conductivity increases more dramatically from 0.56 to $0.63\frac{W}{m\,\mathrm{K}}$. This is due, for the most part, to the change to yellow border with higher thermal conductivity in Figure 14 (b) being able to conduct heat from the source across the entire region of $0.5\le y\le1$. Conversely, in Figure 14 (a) the heat across the region $0\le y\le0.5$ at x=0 is not connected to a yellow pathway.

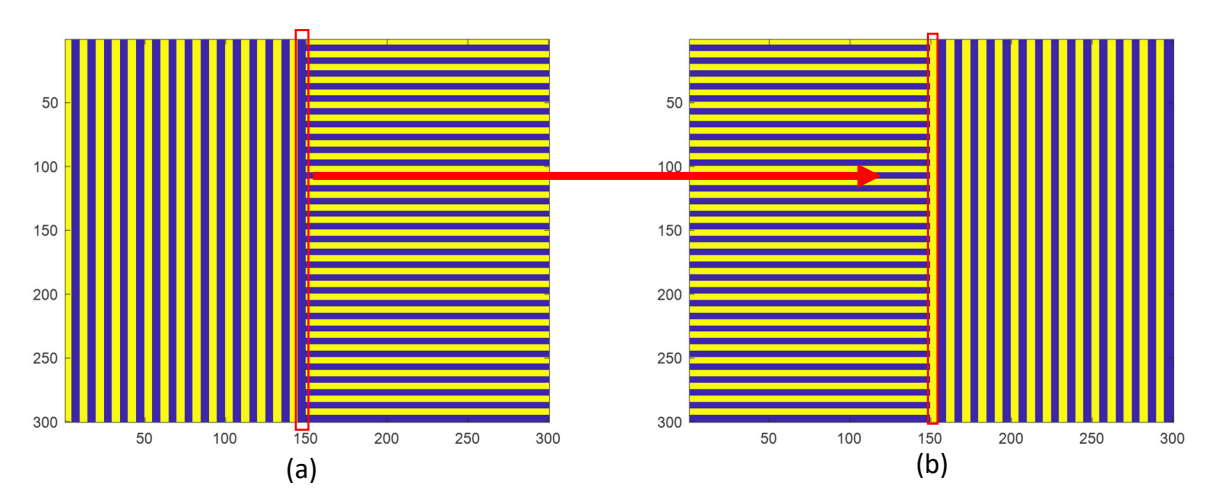


Figure 13. (a) $2 \times 2(4)$ structure; (b) 2×2 (6) structure

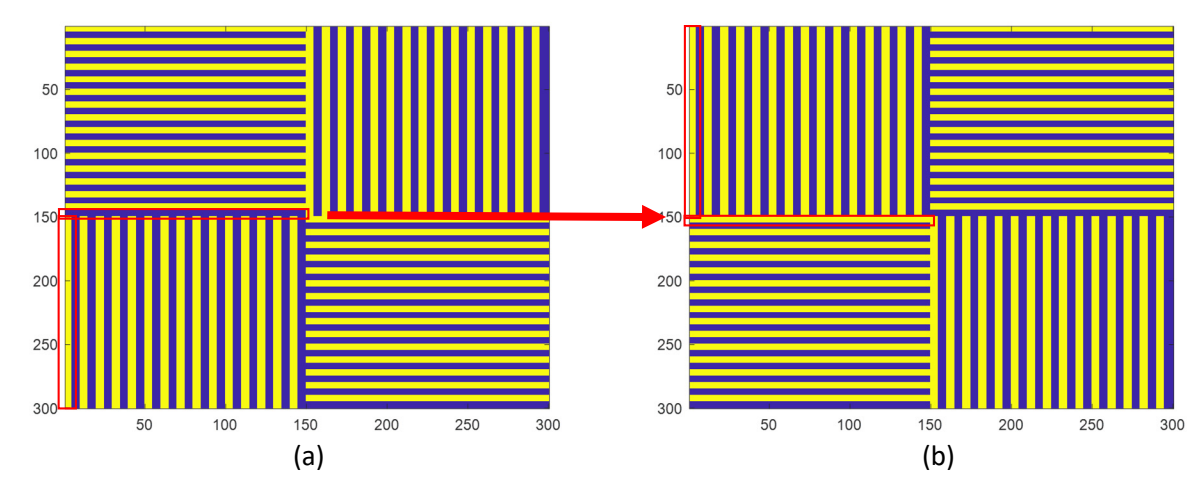


Figure 14. (a) $2 \times 2(1)$ structure; (b) $2 \times 2(2)$ structure

To study the effect of varying the phase contrast, the thermal conductivity of phase A was varied so that $\frac{k_A}{k_B}$ was 3, 10, or 100. The 6 × 6 structure in Figure 9 (a) was used for all cases in this study. The results of

this study are shown in Table 6. In the first scenario with $\frac{k_A}{k_B}=3$, the effective thermal conductivity calculated from FDM is $0.35\frac{W}{m\,\mathrm{K}}$. Sax and Ottino's EMT expression predicts $k_{SPA}=0.35\frac{W}{m\,\mathrm{K}}$ for this case, as does the geometric mean of series and parallel, k_{SPG} . For the second scenario $\frac{k_A}{k_B}=10$, the effective thermal conductivity calculated from FDM is $0.64\frac{W}{m\,\mathrm{K}}$. Sax and Ottino's EMT predicts $k_{SPA}=0.73\frac{W}{m\,\mathrm{K}}$ for this case, while $k_{SPG}=0.63$. For the last case $\frac{k_A}{k_B}=100$, the effective thermal conductivity calculated from FDM is $2.1\frac{W}{m\,\mathrm{K}}$. Sax and Ottino's expression predicts $k_{SPA}=5.25\frac{W}{m\,\mathrm{K}}$, and $k_{SPG}=2.0$. Torquato reports that EMT expressions over predict k_{eff} except when $\frac{k_A}{k_B}$ is small.[80] Over prediction of EMT has been observed experimentally for gas transport through lamellar block copolymers.[37] The results of FDM calculations agree with these findings and indicate that the geometric mean of series and parallel configurations, i.e. k_{SPG} , is a better predictor than Sax and Ottino's EMT expression, at least for lamellar structures with significant phase contrast.

Table 6. Results of phase contrast study, in which k_a/k_b was varied. Predictions from various effective medium expressions are also shown. (All units are in W/m K).

			FDM	Parallel	Series	ЕМТ	Geometric Mean
k_A	k_B	k_A/k_B	k_{eff}	$k_{parallel}$	k_{series}	k_{SPA}	k_{SPG}
0.6	0.2	3	0.35	0.40	0.30	0.35	0.35
2	0.2	10	0.64	1.1	0.36	0.73	0.63
20	0.2	100	2.1	10.1	0.40	5.25	2.00

IV. Conclusions

The effects of grain size, grain boundary connectivity, and phase contrast were evaluated with numerical simulations of 2D lamellar structures, and the best EMT prediction for such structures was identified. A validation of the model is shown by applying the Finite Difference Method to Homogeneous, Series and Parallel structures, where the results of FDM and analytical expressions agreed. A calculation of the thermal conductivity of the diagonal form gives an idea of how heat transport and effective thermal conductivity are affected by rotation of the grain. A set of different grain sizes has been modeled starting with 4 grains up to 225 grains with random orientation to see the impact of the grain size on effective thermal conductivity. Specific manifestations of random structures with large grains, in which the grain is a significant fraction of the transport length, were examined. The connectivity of the more conductive phase at the boundary of large grains can dramatically impact the effective thermal conductivity. The variation in effective thermal conductivity is much greater in large grain structures than in small grain structures, which agrees with experimental observations of ionic conductivity in plastic crystals. Thus, alignment of grains in the direction of desired transport is expected to have a greater effect in large grains than in small grains, and EMT predictions are expected to be less useful for large-grain structures. In general, the predicted thermal conductivity from Sax and Ottino's EMT expression is higher than that calculated from the FDM simulations that explicitly account for specific structures. On the other hand, a geometric average of the series and parallel thermal conductivities accurately predicts the average simulation results. The geometric mean prediction indicates that a completely non-conductive phase would result in no conduction in the limit of small randomly oriented grains. In other words, orders of magnitude improvement due to alignment is entirely possible in the context of the recursive average prediction for lamellar structures. On the other hand, by using solely the arithmetic mean of series and parallel, the Sax and Ottino expression underweights the detrimental impact of the more poorly conducting phase. Increasing contrast between the transport properties of the phases exacerbates this disagreement. A key component of the FDM model is a general flux expression that handles structured control volumes automatically, only requiring a matrix of transport parameters for each position in the control volume. The flux expression is powerful because it can handle any structure that can be represented in a matrix of transport parameters. This FDM model could readily be extended to account for interfacial resistance, 3D transport, and anisotropic transport properties within a phase (for application to 2D materials). It could also be easily adapted to types of transport other than heat. For future work, an investigation on more complex heat sources, boundary conditions, and structures (like cylinders and spheres) would be interesting.

V. <u>Acknowledgment</u>

O. Taleb and D. Hallinan acknowledge NSF for support (NSF Award # 1751450).

V. References

- [1] Y. Yi, X.F. Yu, W.H. Zhou, J.H. Wang, P.K. Chu, Two-dimensional black phosphonts: Synthesis, modification, properties, and applications, Materials Science & Engineering R-Reports, 120 (2017) 1-33.
- [2] A.S. Michaels, H.J. Bixler, FLOW OF GASES THROUGH POLYETHYLENE, Journal of Polymer Science, 50(154) (1961) 413-&.
- [3] H.P. Wang, J.K. Keum, A. Hiltner, E. Baer, Confined Crystallization of PEO in Nanolayered Films Impacting Structure and Oxygen Permeability, Macromolecules, 42(18) (2009) 7055-7066.
- [4] C.L. Choy, D. Greig, The low-temperature thermal conductivity of a semi-crystalline polymer, polyethylene terephthalate, Journal of Physics C: Solid State Physics, 8(19) (1975) 3121-3130.
- [5] P.A. Klonos, S.N. Tegopoulos, C.S. Koutsiara, E. Kontou, P. Pissis, A. Kyritsis, Effects of CNTs on thermal transitions, thermal diffusivity and electrical conductivity in nanocomposites: comparison between an amorphous and a semicrystalline polymer matrix, Soft Matter, 15(8) (2019) 1813-1824.
- [6] S. Gupta, J.D. Schieber, D.C. Venerus, Anisotropic thermal conduction in polymer melts in uniaxial elongation flows, Journal of Rheology, 57(2) (2013) 427-439.
- [7] T. Kato, N. Mizoshita, K. Kishimoto, Functional Liquid-Crystalline Assemblies: Self-Organized Soft Materials, Angewandte Chemie International Edition, 45(1) (2006) 38-68.
- [8] H. Feng, X. Lu, W. Wang, N.-G. Kang, J.W. Mays, Block copolymers: Synthesis, self-assembly, and applications, Polymers, 9(10) (2017) 494.
- [9] S.K. Kumar, R. Krishnamoorti, Nanocomposites: Structure, Phase Behavior, and Properties, Annual Review of Chemical and Biomolecular Engineering, 1(1) (2010) 37-58.
- [10] X.-B. Cheng, R. Zhang, C.-Z. Zhao, Q. Zhang, Toward Safe Lithium Metal Anode in Rechargeable Batteries: A Review, Chemical Reviews, 117(15) (2017) 10403-10473.
- [11] M. Shtein, R. Nadiv, M. Buzaglo, O. Regev, Graphene-Based Hybrid Composites for Efficient Thermal Management of Electronic Devices, ACS Applied Materials & Interfaces, 7(42) (2015) 23725-23730.
- [12] M.L. Mu, C.Y. Wan, T. McNally, Thermal conductivity of 2D nano-structured graphitic materials and their composites with epoxy resins, 2d Materials, 4(4) (2017).
- [13] L.F. Gao, C. Li, W.C. Huang, S. Mei, H. Lin, Q. Ou, Y. Zhang, J. Guo, F. Zhang, S.X. Xu, H. Zhang, MXene/Polymer Membranes: Synthesis, Properties, and Emerging Applications, Chemistry of Materials, 32(5) (2020) 1703-1747.
- [14] H.F. Song, J.M. Liu, B.L. Liu, J.Q. Wu, H.M. Cheng, F.Y. Kang, Two-Dimensional Materials for Thermal Management Applications, Joule, 2(3) (2018) 442-463.
- [15] X. Zhang, X.Y. Zhao, T.T. Xue, F. Yang, W. Fan, T.X. Liu, Bidirectional anisotropic polyimide/bacterial cellulose aerogels by freeze-drying for super-thermal insulation, Chemical Engineering Journal, 385 (2020).
- [16] L. Jing, K.R. Li, H.T. Yang, P.Y. Chen, Recent advances in integration of 2D materials with soft matter for multifunctional robotic materials, Materials Horizons, 7(1) (2020) 54-70.
- [17] D.J. Kinning, E.L. Thomas, J.M. Ottino, Effect of morphology on the transport of gases in block copolymers, Macromolecules, 20(5) (1987) 1129-1133.
- [18] O. Oparaji, M. Minelli, C. Zhu, E. Schaible, A. Hexemer, D.T. Hallinan Jr, Effect of block copolymer morphology on crystallization and water transport, Polymer, 120 (2017) 209-216.
- [19] M. Singh, O. Odusanya, G.M. Wilmes, H.B. Eitouni, E.D. Gomez, A.J. Patel, V.L. Chen, M.J. Park, P. Fragouli, H. latrou, N. Hadjichristidis, D. Cookson, N.P. Balsara, Effect of molecular weight on the mechanical and electrical properties of block copolymer electrolytes, Macromolecules, 40(13) (2007) 4578-4585.
- [20] G.H. Fredrickson, F.S. Bates, Dynamics of block copolymers: Theory and experiment, Annual Review of Materials Science, 26 (1996) 501-550.

- [21] N. Mehra, L. Mu, T. Ji, X. Yang, J. Kong, J. Gu, J. Zhu, Thermal transport in polymeric materials and across composite interfaces, Applied Materials Today, 12 (2018) 92-130.
- [22] A. El Sachat, J. Spiece, C. Evangeli, A.J. Robson, M. Kreuzer, M.R. Rodríguez-Laguna, E. Chavez, M. Sledzinska, C.M. Sotomayor Torres, O.V. Kolosov, Nanoscale mapping of thermal and mechanical properties of bare and metal-covered self-assembled block copolymer thin films, ACS Applied Polymer Materials, 2(2) (2019) 487-496.
- [23] M.C. George, M.A. Rodriguez, M.S. Kent, G.L. Brennecka, P.E. Hopkins, Thermal conductivity of self-assembling symmetric block copolymer thin films of polystyrene-block-poly (methyl methacrylate), Journal of Heat Transfer, 138(2) (2016).
- [24] J.J. Chiu, B.J. Kim, E.J. Kramer, D.J. Pine, Control of nanoparticle location in block copolymers, Journal of the American Chemical Society, 127(14) (2005) 5036-5037.
- [25] M. Al-Hussein, W.H. de Jeu, Crystallization-induced order in polystyrene-poly(ethylene oxide) metallo-supramolecular diblock copolymer, Polymer, 50(9) (2009) 2149-2153.
- [26] M.K. Mayeda, W.-F. Kuan, W.-S. Young, J.A. Lauterbach, T.H. Epps, III, Controlling Particle Location with Mixed Surface Functionalities in Block Copolymer Thin Films, Chemistry of Materials, 24(14) (2012) 2627-2634.
- [27] T. Wagner, J. Lazar, U. Schnakenberg, A. Böker, In situ Electrochemical Impedance Spectroscopy of Electrostatically Driven Selective Gold Nanoparticle Adsorption on Block Copolymer Lamellae, ACS Applied Materials & Interfaces, 8(40) (2016) 27282-27290.
- [28] R.B. Thompson, V.V. Ginzburg, M.W. Matsen, A.C. Balazs, Predicting the Mesophases of Copolymer-Nanoparticle Composites, Science, 292(5526) (2001) 2469-2472.
- [29] B.J. Kim, J. Bang, C.J. Hawker, J.J. Chiu, D.J. Pine, S.G. Jang, S.-M. Yang, E.J. Kramer, Creating surfactant nanoparticles for block copolymer composites through surface chemistry, Langmuir, 23(25) (2007) 12693-12703.
- [30] R.A. Segalman, Patterning with block copolymer thin films, Materials Science and Engineering: R: Reports, 48(6) (2005) 191-226.
- [31] H. Ahn, M.J. Park, Facile One-Pot Synthesis of Functional Gold Nanoparticle—Polymer Hybrids Using Ionic Block Copolymers as a Nanoreactor, Macromolecular Rapid Communications, 32(22) (2011) 1790-1797.
- [32] N. Hoda, L. Budama, B.A. Cakir, O. Topel, R. Ozisik, Fabrication of platinum nanoparticles in aqueous solution and solid phase using amphiphilic PB-b-PEO copolymer nanoreactors, Materials Research Bulletin, 48(9) (2013) 3183-3188.
- [33] P. Kofinas, R.E. Cohen, A.F. Halasa, Gas permeability of polyethylene/poly(ethylene-propylene) semicrystalline diblock copolymers, Polymer, 35(6) (1994) 1229-1235.
- [34] M. Minelli, M.G. Baschetti, D.T. Hallinan, Jr., N.P. Balsara, Study of gas permeabilities through polystyrene-block-poly(ethylene oxide) copolymers, Journal of Membrane Science, 432 (2013) 83-89.
- [35] Y.A. Elabd, C.W. Walker, F.L. Beyer, Triblock copolymer ionomer membranes: Part II. Structure characterization and its effects on transport properties and direct methanol fuel cell performance, Journal of Membrane Science, 231(1) (2004) 181-188.
- [36] J.H. Petropoulos, A COMPARATIVE-STUDY OF APPROACHES APPLIED TO THE PERMEABILITY OF BINARY COMPOSITE POLYMERIC MATERIALS, Journal of Polymer Science Part B-Polymer Physics, 23(7) (1985) 1309-1324.
- [37] J. Csernica, R.F. Baddour, R.E. Cohen, Gas permeability of a polystyrene/polybutadiene block copolymer possessing a misoriented lamellar morphology, Macromolecules, 22(3) (1989) 1493-1496.
- [38] R. Landauer, Electrical conductivity in inhomogeneous media, AIP Conference Proceedings, 40(1) (1978) 2-45.
- [39] K. Pietrak, T.S. Wiśniewski, A review of models for effective thermal conductivity of composite materials, Journal of Power Technologies, (1) (2014) 14-24%V 95.

- [40] J.J. Caruso, C.C. Chamis, Assessment of simplified composite micromechanics using three-dimensional finite-element analysis, Journal of Composites, Technology and Research, 8(3) (1986) 77-83.
- [41] A. Leach, The thermal conductivity of foams. I. Models for heat conduction, Journal of Physics D: Applied Physics, 26(5) (1993) 733.
- [42] J. Sax, J. Ottino, Modeling of transport of small molecules in polymer blends: application of effective medium theory, Polymer Engineering & Science, 23(3) (1983) 165-176.
- [43] V. Premnath, A model for the permeation of gases in block copolymer membranes with lamellar morphology, Journal of Membrane Science, 110(1) (1996) 133-137.
- [44] D.T. Hallinan, I. Villaluenga, N.P. Balsara, Polymer and composite electrolytes, MRS Bulletin, 43(10) (2018) 759-767.
- [45] D. Hallinan, N. Balsara, Annual Review of Materials Research, in: Annual Reviews, Palo Alto, 2013.
- [46] S. Cheng, D.M. Smith, C.Y. Li, How Does Nanoscale Crystalline Structure Affect Ion Transport in Solid Polymer Electrolytes?, Macromolecules, 47(12) (2014) 3978-3986.
- [47] S. Cheng, D.M. Smith, Q. Pan, S. Wang, C.Y. Li, Anisotropic ion transport in nanostructured solid polymer electrolytes, RSC Advances, 5(60) (2015) 48793-48810.
- [48] S. Cheng, D.M. Smith, C.Y. Li, Anisotropic Ion Transport in a Poly(ethylene oxide)—LiClO4 Solid State Electrolyte Templated by Graphene Oxide, Macromolecules, 48(13) (2015) 4503-4510.
- [49] D.M. Smith, S. Cheng, W. Wang, T.J. Bunning, C.Y. Li, Polymer electrolyte membranes with exceptional conductivity anisotropy via holographic polymerization, Journal of Power Sources, 271 (2014) 597-603.
- [50] D.M. Smith, Q. Pan, S. Cheng, W. Wang, T.J. Bunning, C.Y. Li, Nanostructured, Highly Anisotropic, and Mechanically Robust Polymer Electrolyte Membranes via Holographic Polymerization, Advanced Materials Interfaces, 5(1) (2018) 1700861.
- [51] K. Romanenko, L. Jin, L.A. Madsen, J.M. Pringle, L.A. O'Dell, M. Forsyth, Anisotropic MRI Contrast Reveals Enhanced Ionic Transport in Plastic Crystals, Journal of the American Chemical Society, 136(44) (2014) 15638-15645.
- [52] T. Ohtake, M. Ogasawara, K. Ito-Akita, N. Nishina, S. Ujiie, H. Ohno, T. Kato, Liquid-Crystalline Complexes of Mesogenic Dimers Containing Oxyethylene Moieties with LiCF3SO3: Self-Organized Ion Conductive Materials, Chemistry of Materials, 12(3) (2000) 782-789.
- [53] K. Kishimoto, T. Suzawa, T. Yokota, T. Mukai, H. Ohno, T. Kato, Nano-Segregated Polymeric Film Exhibiting High Ionic Conductivities, Journal of the American Chemical Society, 127(44) (2005) 15618-15623.
- [54] Y. Wang, Y. Chen, J. Gao, H.G. Yoon, L. Jin, M. Forsyth, T.J. Dingemans, L.A. Madsen, Highly Conductive and Thermally Stable Ion Gels with Tunable Anisotropy and Modulus, Advanced Materials, 28(13) (2016) 2571-2578.
- [55] R. Mäki-Ontto, K. de Moel, E. Polushkin, G. Alberda van Ekenstein, G. ten Brinke, O. Ikkala, Tridirectional Protonic Conductivity in Soft Materials, Advanced Materials, 14(5) (2002) 357-361.
- [56] M.J. Park, N.P. Balsara, Anisotropic Proton Conduction in Aligned Block Copolymer Electrolyte Membranes at Equilibrium with Humid Air, Macromolecules, 43(1) (2010) 292-298.
- [57] Y.A. Elabd, E. Napadensky, C.W. Walker, K.I. Winey, Transport properties of sulfonated poly (styrene-b-isobutylene-b-styrene) triblock copolymers at high ion-exchange capacities, Macromolecules, 39(1) (2006) 399-407.
- [58] P.W. Majewski, M. Gopinadhan, C.O. Osuji, The Effects of Magnetic Field Alignment on Lithium Ion Transport in a Polymer Electrolyte Membrane with Lamellar Morphology, Polymers, 11(5) (2019) 887.
- [59] J. Hou, J. Li, L.A. Madsen, Anisotropy and Transport in Poly(arylene ether sulfone) Hydrophilic–Hydrophobic Block Copolymers, Macromolecules, 43(1) (2010) 347-353.
- [60] W.-S. Young, T.H. Epps, Ionic Conductivities of Block Copolymer Electrolytes with Various Conducting Pathways: Sample Preparation and Processing Considerations, Macromolecules, 45(11) (2012) 4689-4697.

- [61] R.L. Weber, Y. Ye, A.L. Schmitt, S.M. Banik, Y.A. Elabd, M.K. Mahanthappa, Effect of Nanoscale Morphology on the Conductivity of Polymerized Ionic Liquid Block Copolymers, Macromolecules, 44(14) (2011) 5727-5735.
- [62] M. Chintapalli, X.C. Chen, J.L. Thelen, A.A. Teran, X. Wang, B.A. Garetz, N.P. Balsara, Effect of Grain Size on the Ionic Conductivity of a Block Copolymer Electrolyte, Macromolecules, 47(15) (2014) 5424-5431.
- [63] M. Chintapalli, T.N.P. Le, N.R. Venkatesan, N.G. Mackay, A.A. Rojas, J.L. Thelen, X.C. Chen, D. Devaux, N.P. Balsara, Structure and Ionic Conductivity of Polystyrene-block-poly(ethylene oxide) Electrolytes in the High Salt Concentration Limit, Macromolecules, 49(5) (2016) 1770-1780.
- [64] K. Timachova, I. Villaluenga, L. Cirrincione, M. Gobet, R. Bhattacharya, X. Jiang, J. Newman, L.A. Madsen, S.G. Greenbaum, N.P. Balsara, Anisotropic Ion Diffusion and Electrochemically Driven Transport in Nanostructured Block Copolymer Electrolytes, The Journal of Physical Chemistry B, 122(4) (2018) 1537-1544.
- [65] H.S. Carslaw, J.C. Jaeger, Conduction of Heat in Solids, Second ed., Oxford University Press, Breat Britain, 1946.
- [66] R. Ash, R.M. Barrer, J.H. Petropoulos, DIFFUSION IN HETEROGENEOUS MEDIA PROPERTIES OF A LAMINATED SLAB, British Journal of Applied Physics, 14(12) (1963) 854-&.
- [67] J. Crank, The Mathematics of Diffusion, Second ed., Oxford University Press, Great Britain, 1975.
- [68] H. Brenner, D.A. Edwards, Macrotransport Processes, Butterworth-Heinemann, Boston, 1993.
- [69] J.R. Bartlit, Heat-transfer calculation by finite differences, George M. Dusinberre, International Textbook Company, Scranton, Pennsylvania (1961). 293 pages, in, Wiley Online Library, 1962.
- [70] T. Narasimhan, P. Witherspoon, An integrated finite difference method for analyzing fluid flow in porous media, Water Resources Research, 12(1) (1976) 57-64.
- [71] H. Claiborne, R. Wagner, R. Just, Comparison of the results of several heat transfer computer codes when applied to a hypothetical nuclear waste repository, Oak Ridge National Lab., TN (USA), 1979.
- [72] T.C. Choy, Effective Medium Theory: Principles and Applications, Oxford University Press, 2016.
- [73] Y. Gao, Y. Zhou, X. Zhang, M. Hu, Extremely Low Thermal Conductivity of Polycrystalline Silicene, The Journal of Physical Chemistry C, 122(16) (2018) 9220-9228.
- [74] B. Wu, Y. Zhou, M. Hu, Two-Channel Thermal Transport in Ordered–Disordered Superionic Ag₂Te and Its Traditionally Contradictory Enhancement by Nanotwin Boundary, The Journal of Physical Chemistry Letters, 9(19) (2018) 5704-5709.
- [75] R.G. Rice, D.D. Do, Applied mathematics and modeling for chemical engineers, John Wiley & Sons, 2012.
- [76] P.S. Bullen, The Arithmetic, Geometric and Harmonic Means, in: Handbook of Means and Their Inequalities, Springer Netherlands, Dordrecht, 2003, pp. 60-174.
- [77] B.C. Carlson, Algorithms Involving Arithmetic and Geometric Means, The American Mathematical Monthly, 78(5) (1971) 496-505.
- [78] D.R. Chaudhary, R.C. Bhandari, Heat transfer through a three-phase porous medium, Journal of Physics D: Applied Physics, 1(6) (1968) 815-817.
- [79] W. Woodside, J.H. Messmer, Thermal Conductivity of Porous Media. I. Unconsolidated Sands, Journal of Applied Physics, 32(9) (1961) 1688-1699.
- [80] S. Torquato, H. Haslach Jr, Random heterogeneous materials: microstructure and macroscopic properties, Appl. Mech. Rev., 55(4) (2002) B62-B63.
- [81] W.M. Deen, Analysis of transport phenomena, Oxford university press New York, 1998.

Derivation of Equation 7

Appendix A

Consider 2 nodes: A in yellow and B in blue. The temperature at A is T_A , and the temperature at B is T_B . The temperature at the A/B interface is T_{int} . Imposing flux matching at the interface, i.e. there is no accumulation nor consumption/generation at the interface, yields

$$q^{-} = q^{+} \text{ (A1)}$$

$$-k_{A} \nabla T_{A} = -k_{A} \frac{(T_{int} - T_{A})}{\Delta x/2} = -k_{B} \frac{(T_{B} - T_{int})}{\Delta x/2} = -k_{B} \nabla T_{B} \text{ (A2)}$$

$$k_{A} T_{A} + k_{B} T_{B} = k_{A} T_{int} + k_{B} T_{int} \text{ (A3)}$$

$$T_{int} = \frac{k_{A} T_{A} + k_{B} T_{B}}{k_{A} + k_{B}} \text{ (A4)}$$

$$\nabla T = \frac{T_{B} - T_{A}}{\Delta x} = \frac{T_{B} - T_{int} + T_{int} - T_{A}}{\Delta x} = \frac{1}{2} \left[\frac{(T_{B} - T_{int})}{\Delta x/2} + \frac{(T_{int} - T_{A})}{\Delta x/2} \right] \text{ (A5)}$$

Solving the gradient in the A phase by substituting for T_{int}

$$\nabla T_A = \frac{(T_{int} - T_A)}{\Delta x/2} = \frac{\left(\frac{k_A T_A + k_B T_B}{k_A + k_B} - T_A\right)}{\Delta x/2} = \frac{k_B}{k_A + k_B} \frac{(T_B - T_A)}{\Delta x/2}$$
(A6)

Similarly, the gradient in the B phase is

$$\nabla T_B = \frac{k_A}{k_A + k_B} \frac{(T_B - T_A)}{\Delta x/2} \text{ (A7)}$$

From equation A5 the gradient between the two nodes is

$$\nabla T = \frac{\nabla T_A + \nabla T_B}{2} = \frac{k_A + k_B}{k_A + k_B} \frac{(T_B - T_A)}{\Delta x} = \frac{(T_B - T_A)}{\Delta x}$$

Since $q = q^- = q^+$,

$$q=-k_A
abla T_A=-k_B
abla T_B$$
 , or
$$q=-rac{2k_Ak_B}{k_A+k_B}rac{T_B-T_A}{\Delta x}$$
 ,

which is equation 7.

Appendix A

Derivation of Equation 16

First, a non-dimensionalization of the governing equation is required to simplify the solution, where T_W and T_0 are stated in the boundary conditions, $W = 10^{-4}$.

$$\Theta = \frac{T - T_W}{T_0 - T_W} \qquad \qquad \xi = \frac{x}{W} \qquad \qquad \tau = \frac{t}{t^*}$$

Plugging the new change of variables in equation 15

$$\rho C_P \frac{(T_0 - T_W) \partial \Theta}{t^* \partial \tau} = k(T_0 - T_W) \frac{\partial^2 \Theta}{W^2 \partial \xi^2}$$

Since $t^* = \frac{W^2 \rho C_P}{k}$

$$\frac{\partial \Theta}{\partial \tau} = \frac{\partial^2 \Theta}{\partial \xi^2}$$
 (A8)

The non-dimensionalized governing equation is equation A8, and the new boundaries conditions relative to the new variables are shown below.

$$\xi = 0$$
 $\Theta = 1$

$$\xi = 1$$
 $\Theta = 0$

$$\tau = 0$$
 $\Theta = 0$

As shown in Deen's book, the solution for this case is a Fourier series solution of the following form [81]

$$\Theta(\xi,\tau) = \sum \psi(\tau)\Phi(\xi) \text{ (A9)}$$

 $\psi(\tau)$ is the time dependent solution and $\Phi(\xi)$ is the basis function. Based on 2 Dirichlet boundary conditions, the basis function is defined by $\Phi(\xi) = \sqrt{2} \sin(n\pi\xi)$, and the derivative of the basis function is $\frac{d\Phi(\xi)}{d\xi} = \sqrt{2}n\pi\cos(n\pi\xi)$. The partial differential equation (PDE) and the boundaries condition are transformed to an ordinary differential equation (ODE) by integrating over the control volume with respect to the dependent variable of the basis function.

$$\int_{0}^{1} \Phi(\xi) \left[\frac{\partial \Theta}{\partial \tau} - \frac{\partial^{2} \Theta}{\partial \xi^{2}} \right] d\xi = 0 \text{ (A10)}$$

The time dependent function results from this finite Fourier Transform.

$$\int_0^1 \Phi(\xi) \,\Theta(\xi,\tau) d\xi = \psi(\tau) \,(A11)$$

Each term of equation A10 is integrated in turn. The first term is

$$\frac{\partial}{\partial \tau} \int_0^1 \Phi(\xi) \, \Theta(\xi, \tau) d\xi = \frac{\partial \psi(\tau)}{\partial \tau}.$$

The second term requires 2 integration by parts.

Appendix A

$$\int_{0}^{1} \Phi(\xi) \frac{\partial^{2} \Theta}{\partial \xi^{2}} d\xi = \left[\Phi \frac{\partial \Theta}{\partial \xi} - \frac{\partial \Phi}{\partial \xi} \Theta \right]_{0}^{1} + \int_{0}^{1} \Theta \frac{\partial^{2} \Phi}{\partial \xi^{2}} d\xi$$

applying the boundary conditions $\Phi(0) = 0 = \Phi(1) = \Theta(1)$, and $\Theta(0) = 1$.

$$\int_0^1 \Phi(\xi) \frac{\partial^2 \Theta}{\partial \xi^2} d\xi = \sqrt{2} n\pi - (n\pi)^2 \psi(\tau)$$
 (A12)

Substituting equations A11 and A12 into A10, the PDE is transformed to an ODE, and the non-homogenous boundary condition is incorporated into the transformed PDE as a non-homogenous term.

$$\frac{\partial \psi(\tau)}{\partial \tau} + (n\pi)^2 \psi(\tau) = \sqrt{2}n\pi \text{ (A13)}$$

With the initial condition $\psi(0)=0$, the solution of equation A13 is

$$\psi(\tau) = \frac{\sqrt{2}}{n\pi} \left(1 - e^{-(n\pi)^2 \tau} \right) (A14)$$

Combining equation A14 and the basis function in equation A9 yields

$$\Theta(\xi,\tau) = \sum \psi(\tau)\Phi(\xi) = 2\sum \frac{\sin(n\pi\xi)}{n\pi} \left(1 - e^{-(n\pi)^2\tau}\right) (A15)$$

Finally, the steady-state solution should be involved in the solution, where $\frac{\partial^2 \Theta}{\partial \xi^2} = 0$. The solution of the steady-state case after applying the boundary condition is $\Theta_{ss} = 1 - \xi$. Transforming the steady state solution to recognize it in the Fourier series solution, $\int_0^1 \Phi(\xi) \, \Theta_{ss} d\xi = \frac{\sqrt{2}}{n\pi}$, so $\Theta_{ss} = 2 \sum \frac{\sin(n\pi\xi)}{n\pi}$. The final solution analytically expressed exactly for the steady-state part and as an infinite series for the transient part is

$$\Theta(\xi, \tau) = \sum \psi(\tau) \Phi(\xi) = (1 - \xi) - 2 \sum \frac{\sin(n\pi\xi)}{n\pi} e^{-(n\pi)^2 \tau}$$
(A16)

Replace each term in equation A16 by its corresponding variable defined earlier in this section to find the final solution of the temperature profile,

$$\frac{T - T_W}{T_0 - T_W} = (1 - \frac{x}{W}) - 2\sum \frac{\sin(n\pi \frac{x}{W})}{n\pi} e^{-(n\pi)^2 \frac{t}{t^*}}$$
(A17)

Appendix B

Table B1. Summary of FDM results, including average flux at x=0 (Q1) and at x=1 (Q2) and their

percent difference (% diff), as well as effective thermal conductivity and structure.

Grain size*	Q1 W/cm ²	Q2 W/cm ²	% diff	k_{eff} W/m K	$\langle k_{eff} \rangle$ W/m K	Standard deviation	Structure	Predicted k_{eff}
1 × 1	15050	15050	0	2.0	-	-	Homogeneous	2.0 (k _A)
1×1	2736.4	2736.4	0	0.36	-	-	Vertical	$0.36 (k_{series})$
1×1	8277.7	8277.7	0	1.1	-	-	Horizontal	$1.1 (k_{parallel})$
1×1	4674	4563.2	2.37	0.61	-	-	Diagonal	-
1 × 1(2)	4781.1	4702.1	1.65	0.62	-	-	Diagonal 10 τ	0.63 (k _{SPG})
2 × 2 (1)	4225.7	4226.8	0.026	0.56				
2 × 2 (2)	4729.4	4759.4	0.63	0.63				
2 × 2 (3)	4729.4	4759.4	0.63	0.63	0.64	0.12	Random Grains	$0.63 (k_{SPG})$
2 × 2 (4)	4082.5	4082.3	0.004	0.54]			
2 × 2 (5)	6333.2	6349.6	0.26	0.84				
3 × 3 (1)	5380.3	5363.4	0.31	0.71				
3 × 3 (2)	4508.4	4525.3	0.37	0.60]			
3 × 3 (3)	5278.7	5295.1	0.31	0.70	0.656	0.10	Random Grains	0.63 (k _{SPG})
3 × 3 (4)	3822.6	3841.9	0.5	0.51	1			
3 × 3 (5)	5689	5689.8	0.015	0.76				
5 × 5(1)	4442.1	4439.4	0.0607	0.59				
5 × 5(2)	3813.9	3819.4	0.14	0.51				
5 × 5(3)	5161.9	5166.2	0.08	0.69	0.636	0.10	Random Grains	0.63 (k _{SPG})
5 × 5(4)	5700.2	5709.6	0.16	0.76				. 5. 67
5 × 5(5)	4761.2	4724.8	0.76	0.63	1			
6 × 6 (1)	4808.7	4808.4	0.0062	0.64				
6 × 6 (2)	4225.7	4226.8	0.026	0.56	1			
6 × 6(3)	4831.9	4855.7	0.49	0.65	0.624	0.05	Random Grains	$0.63 (k_{SPG})$
6 × 6(4)	5249.7	5234.5	0.29	0.69	1			
6 × 6(5)	4336.3	4339.8	0.08	0.58				
10 × 10(1)	5099.7	5113	0.26	0.68				
10 × 10(2)	4873.1	4862.2	0.22	0.65				
10 × 10(3)	4789.8	4813.4	0.49	0.64	0.672	0.025	Random Grains	0.63 (k _{SPG})
10 × 10(4)	5183.2	5188.4	0.1	0.69	1			
10 × 10(5)	5208.8	5225.5	0.32	0.70				
15 × 15(1)	4742.8	4738.6	0.08	0.63				
15 × 15(2)	4577.5	4601.5	0.52	0.61	1			
15 × 15(3)	4638.5	4669.1	0.66	0.62	0.624	0.011	Random Grains	0.63 (k _{SPG})
15 × 15(4)	4803.1	4809.6	0.14	0.64	1			
15 × 15(5)	4650.8	4650.9	0.0021	0.62	1			

Appendix B

* The number in parentheses in the first column refers to the trial number. The first column entry is used to label each structure in the Supporting Information.